The Astronomical Journal, 130:2019–2042, 2005 November

OPTICAL IDENTIFICATION OF *INFRARED SPACE OBSERVATORY* FAR-INFRARED SOURCES IN THE LOCKMAN HOLE USING A DEEP VERY LARGE ARRAY 1.4 GHz CONTINUUM SURVEY

S. Oyabu,[1,2,3] Min S. Yun,[2,4] T. Murayama,[5] D. B. Sanders,[6] K. Kawara,[1] Y. Taniguchi,[5] S. Veilleux,[7] H. Okuda,[8,9] H. Matsuhara,[8] L. L. Cowie,[6] Y. Sato,[2,10] K. Wakamatsu,[11] and Y. Sofue[1]

Received 2005 January 19; accepted 2005 July 2

ABSTRACT

By exploiting the far-infrared (FIR) and radio correlation, we have performed a likelihood-ratio analysis to identify optical counterparts to the FIR sources that have been found in an area of $\sim$0.9 deg^2 during the *Infrared Space Observatory* (*ISO*) deep FIR survey in the Lockman Hole. New ground-based observations have been conducted to build up the catalogs of radio and optical objects, which include a deep Very Large Array (VLA) observation at 1.4 GHz, optical *R*- and *I*-band imaging with the Subaru 8 m and University of Hawaii 2.2 m telescopes, and optical spectroscopy with the Keck II 10 m and WIYN 3.5 m telescopes. This work is based on FIR samples consisting of 116 and 20 sources selected with the criteria of $F^C(90\ \mu\mathrm{m}) \geq 43$ mJy and $F^C(170\ \mu\mathrm{m}) \geq 102$ mJy, respectively, where F^C is the bias-corrected flux. Using the likelihood ratio analysis and the associated reliability, 44 FIR sources have been identified with radio sources. Optical confirmation of the 44 FIR/radio associations was then conducted using accurate radio positions. Redshifts have been obtained for 29 out of the 44 identified sources. One hyperluminous infrared galaxy (HyLIRG) with $L_{\mathrm{FIR}} > 10^{13}\ L_\odot$ and four ultraluminous infrared galaxies (ULIRGs) with $L_{\mathrm{FIR}} = 10^{12}$–$10^{13}\ L_\odot$ are identified in our sample, while the remaining 24 FIR galaxies have $L_{\mathrm{FIR}} < 10^{12}\ L_\odot$. The space density of the FIR sources at $z = 0.3$–0.6 is 4.6×10^{-5} Mpc^{-3}, which is 460 times larger than the local value, implying a rapid evolution of the ULIRG population. Most *ISO* FIR sources have $L(1.4\ \mathrm{GHz})/L(90\ \mu\mathrm{m})$ similar to the star-forming galaxies Arp 220 and M82, indicating that star formation is the dominant mechanism for their FIR and radio luminosity.

At least seven of our FIR sources show evidence for the presence of an active galactic nucleus (AGN) in optical emission lines, radio continuum excess, or X-ray activity. Three out of five (60%) of the ULIRGs/HyLIRGs are AGN galaxies, suggesting that the AGN fraction among the ULIRG/HyLIRG population may not change significantly between $z \sim 0.5$ and the present epoch. Five of the seven AGN galaxies are within the *ROSAT* X-ray survey field, and two are within the *XMM-Newton* survey fields. X-ray emission has been detected in only one source, 1EX030, which is optically classified as a quasar. The nondetection in the *XMM-Newton* 2–10 keV band suggests a very thick absorption column density of 3×10^{24} cm^{-2} or $A_V \sim 1200$ mag obscuring the central source of the two AGN galaxies. Several sources have an extreme FIR luminosity relative to the optical *R* band, $L(90\ \mu\mathrm{m})/L(R) > 500$, which is rare even among the local ULIRG population. While source confusion or blending might offer an explanation in some cases, these observations may represent a new population of galaxies with an extreme amount of star formation in an undeveloped stellar system, i.e., formation of bulges or young elliptical galaxies.

Key words: galaxies: evolution — galaxies: starburst — infrared: galaxies

1. INTRODUCTION

The detection of the far-infrared (FIR) cosmic infrared background (CIRB) radiation by FIRAS and DIRBE on *COBE* was an important step toward understanding the physical properties of the cosmological FIR radiation. The CIRB was interpreted as the emission by dust in distant galaxies (Puget et al. 1996; Fixsen et al. 1998; Hauser et al. 1998), which sets a relevant constraint on the evolution of cosmic sources. The CIRB is 10 times brighter than the expected intensity based on the assumption that the infrared emissivity of galaxies does not change with cosmic time (Takeuchi et al. 2001; Franceschini et al. 2001) and makes a comparable contribution to the total intensity as expected from optical counts from the Hubble Deep Field and the Subaru Deep Field (Totani et al. 2001; Totani & Takeuchi 2002). Therefore, the CIRB's excess suggests that galaxies in the past were much more *active* in the FIR and that a substantial fraction of the total energy emitted by high-redshift galaxies was absorbed by dust and reemitted at long wavelengths.

The SCUBA bolometer camera (Holland et al. 1999) on the submillimeter James Clerk Maxwell Telescope was able to resolve at least half of the CIRB at a wavelength of 850 μm into a population of very luminous infrared galaxies at $z \gtrsim 1$ (Smail et al. 1997; Hughes et al. 1998; Barger et al. 1998; Blain et al.

---

[1] Institute of Astronomy, University of Tokyo, 2-21-1 Osawa, Mitaka, Tokyo 181-0015, Japan.

[2] Visiting Astronomer, WIYN, National Optical Astronomy Observatory (NOAO), which is operated by the Association of Universities for Research in Astronomy (AURA), Inc., under cooperative agreement with the National Science Foundation.

[3] Current address: Institute of Space and Astronautical Science, Japan Aerospace Exploration Agency, 3-1-1 Yoshinodai, Sagamihara, Kanagawa 229-8510, Japan; oyabu@ir.isas.jaxa.jp.

[4] Department of Astronomy, University of Massachusetts, 619 Lederle Graduate Research Center, Amherst, MA 01003.

[5] Astronomical Institute, Tohoku University, Aoba, Sendai 980-77, Japan.

[6] Institute for Astronomy, University of Hawaii, 2680 Woodlawn Drive, Honolulu, HI 96822.

[7] Department of Astronomy, University of Maryland, College Park, MD 20742.

[8] Institute of Space and Astronautical Science, Japan Aerospace Exploration Agency, 3-1-1 Yoshinodai, Sagamihara, Kanagawa 229-8510, Japan.

[9] Gunma Astronomical Observatory, Gunma 377-0702, Japan.

[10] National Astronomical Observatory of Japan, Mitaka, Tokyo 181-8588, Japan.

[11] Faculty of Engineering, Gifu University, Gifu 501-1193, Japan.

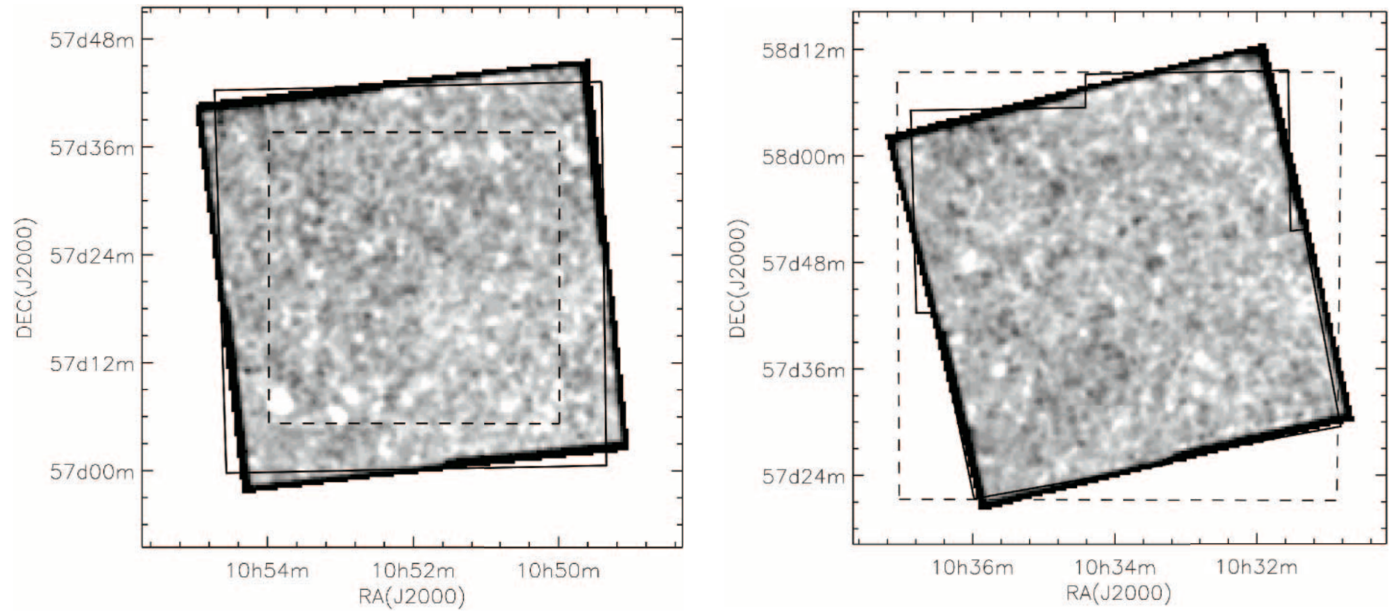

Fig. 1.—Survey areas superposed on the *ISO* 90 μm images in the Lockman Hole. The LHEX field is shown in the left panel, and LHNW on the right. The 170 μm fields are shown by solid lines, while dashed lines present the areas of our VLA 1.4 GHz sources used in this paper.

1999). ISOCAM mid-infrared surveys (Rowan-Robinson et al. 1997; Flores et al. 1999; Mann et al. 2002) have also reported a higher infrared luminosity density (thus a higher star formation rate) at $0.5 \lesssim z \lesssim 1$ than estimated by previous optical studies.

IRAS was able to detect infrared galaxies only to moderate redshifts ($z \sim 0.1$), with the exception of a few hyperluminous and/or lensed objects such as FSC 10214+4724 (Rowan-Robinson et al. 1991). The improvement of the sensitivity and the extension to the longer wavelength (170 μm) in FIR with the ISOPHOT instrument on board the *Infrared Space Observatory* (*ISO*) provides us with a new tool to study FIR emission from galaxies at higher redshifts than those seen by *IRAS*, and the exploration of the "optically dark side" of star formation history through a deep FIR survey was the obvious next step.

The spectral energy distribution (SED) of actively star-forming galaxies peaks at $\lambda \sim 100$ μm. The "negative" *k*-correction makes observations at wavelengths longer than this FIR peak advantageous for detecting high-redshift galaxies. Furthermore, such measurements give the total luminosity without any model-dependent bolometric correction. Therefore, several deep surveys were undertaken with ISOPHOT at 90 and/or 170 μm. We performed a deep FIR survey of two fields in the Lockman Hole region in both the 90 and 170 μm bands as a part of a Japanese/University of Hawaii (UH) cosmology project (Kawara et al. 1998). A 170 μm survey of two fields in the southern Marano area and two fields in the northern European Large-Area *ISO* Survey (ELAIS) with a combined area of 4 deg^2 constitute the FIRBACK program (Puget et al. 1999). A 90 μm survey in ELAIS (Efstathiou et al. 2000) covered 11.6 deg^2.

In order to explore the nature of *ISO* FIR sources in the Lockman Hole fields, we identified counterparts to the sources at optical and radio wavelengths. We obtained their photometric characteristics and measured their redshifts in order to understand the genuine nature of *ISO* FIR sources in the Lockman Hole fields. Section 2 describes the observations and the data, § 3 presents the method and results of the source identification, and § 4 discusses the *ISO* FIR sources in the Lockman Hole fields. The summary is presented in § 5. The Appendix compares our catalogs with those of Rodighiero et al. (2003) and Rodighiero & Franceschini (2004), which reduced the same data with their own method. Throughout the paper, a flat universe with $H_0 = 70$ km s^{-1} Mpc^{-1}, $\Omega_M = 0.3$, and $\Omega_\lambda = 0.7$ is adopted.

2. DATA

2.1. *ISO Far-Infrared Catalogs*

Our FIR survey was performed in the ISOPHOT bands C_90 (90 μm for the reference wavelength) and C_160 (170 μm; see Kawara et al. 1998, 2004; Matsuhara et al. 2000) in the Lockman Hole, where the H I column density is measured to be the lowest in the sky (Lockman et al. 1986), and thus the confusion noise due to the infrared cirrus is expected to be the lowest. The survey includes two fields named LHEX and LHNW, each of which covers approximately $44' \times 44'$ in area. One of the fields, LHEX, was also the target of the *ROSAT* Lockman Hole ultradeep HRI survey (Hasinger et al. 1998). The 90 and 170 μm observations with *ISO* (Kessler et al. 1996) and the data reduction are described in detail by Kawara et al. (1998, 2004). As shown in Figure 1, the ISOPHOT instrument (Lemke et al. 1996) was used to map a total area of ~0.9 deg^2, consisting of two $44' \times 44'$ fields.

The IRAF[12] DAOPHOT package, which was developed to perform stellar photometry in crowded fields (Stetson 1987), was used to perform the source extraction from the FIR maps. The survey images are very crowded, with two or more sources frequently appearing blended. The FWHM measurements show that most bright sources subtend no more than two detector pixels, implying that these sources are detected as point sources. The final 90 and 170 μm source catalogs for signal-to-noise ratios of 3 or greater include 223 and 72 sources, respectively (Kawara et al. 2004). UGC 06009,[13] which is the only *IRAS* source located within our survey fields, was used for the flux scaling assuming $F(90\ \mu\mathrm{m}) = 1218$ mJy and $F(170\ \mu\mathrm{m}) = 1133$ mJy. The flux

---

[12] IRAF is distributed by NOAO, which is operated by AURA, Inc., under contract to the NSF.

[13] If more accurate fluxes are measured in UGC 06009, the fluxes of the FIR sources should be rescaled accordingly.

density of the cataloged sources ranges between 40 and 400 mJy at 90 μm and between 90 and 410 mJy at 170 μm.

The surface number densities of *ISO* FIR sources are sufficiently high (10–20 beams per source) that the derived quantities such as flux, position, completeness, and detection limits are significantly affected by source confusion. To evaluate these effects, Kawara et al. (2004) performed a set of simulations by adding artificial sources to the observed FIR maps. These simulations have shown that the measured fluxes of faint sources are indeed significantly overestimated, and thus, the correction for the flux bias is important. The following expressions are used for the correction:

$$F(90\ \mu\mathrm{m}) = 66 + 0.78F^C(90\ \mu\mathrm{m}) + 0.0001\left[F^C(90\ \mu\mathrm{m})\right]^2, \tag{1}$$

$$F(170\ \mu\mathrm{m}) = 160 + 0.32F^C(170\ \mu\mathrm{m}) + 0.0007\left[F^C(170\ \mu\mathrm{m})\right]^2, \tag{2}$$

where F and F^C denote the observed flux and the flux after correction for the bias effect, respectively. These expressions represent the results from the simulations by Kawara et al. (2004) with 2%–3% accuracy for $F(90\ \mu\mathrm{m}) \geq 100$ mJy or $F(170\ \mu\mathrm{m}) \geq 250$ mJy, and 10% for $F(170\ \mu\mathrm{m}) < 250$ mJy. Thus, the errors resulting from the expressions are small enough to be ignored. In this paper we use the corrected fluxes from equations (1) and (2).

Positional uncertainties are also estimated from these simulations. Position error depends on the brightness of the FIR sources, and the dispersion in the measured position relative to the input position of the artificial sources, σ_{pos}, is larger toward fainter sources. The derived positional uncertainties from the simulations are $\sigma_{\mathrm{pos}}(90\ \mu\mathrm{m}) \sim 20''$ for $F(90\ \mu\mathrm{m}) \sim 100$ mJy and $\sigma_{\mathrm{pos}}(170\ \mu\mathrm{m}) \sim 35''$ for $F(170\ \mu\mathrm{m}) \sim 200$ mJy. Simulations also show that the completeness rapidly decreases as the flux decreases below 200 mJy; for example, the detection rate is 73% for sources with $F^C(90\ \mu\mathrm{m}) = 43$ mJy and 64% for $F^C(170\ \mu\mathrm{m}) = 102$ mJy.

2.2. *Radio Observations*

The *ISO* positional uncertainties of $20''$–$35''$ are too large to search for optical counterparts directly because there are always several faint optical sources within each error circle. Thus, we have taken a two-step approach to identifying FIR sources. In the first step, deep Very Large Array (VLA) 1.4 GHz imaging was performed, and radio counterparts were found using the well-known FIR-radio correlation (Condon 1992; Yun et al. 2001).

This approach may introduce a slight bias in favor of star-forming galaxies, but the active galactic nucleus (AGN)–dominated sources are rare in general in the FIR-selected sample (less than a few percent; see Yun et al. 2001). Once radio counterparts are known, then the positional uncertainty is reduced greatly, to $\leq 1''$, and the second step of searching for optical counterparts becomes straightforward.

Deep 1.4 GHz continuum images of the LHNW and LHEX fields were obtained using the NRAO[14] VLA in the B configuration in 2000 February and 2001 March–April, respectively. Four separate pointings covered a $45' \times 45'$ region centered on the two *ISO* survey fields. The angular resolution of the final images was about $5''$ (FWHM).

The rms noise achieved in the central $32' \times 32'$ mapping region of the LHEX field was $1\ \sigma \sim 15\ \mu$Jy. After combining additional data from the archive, the rms noise in the northeast quadrant centered near the *ROSAT* Deep Survey field (Hasinger et al. 1998) improved to $1\ \sigma \sim 10\ \mu$Jy. Our new VLA 1.4 GHz continuum image has about 2–3 times higher angular resolution and improved sensitivity over the previous observations by de Ruiter et al. (1997): $\theta \sim 12''$ and $1\ \sigma \sim 30\ \mu$Jy.

In the LHNW field, four separate pointings were also used. However, the imaging dynamic range in the LHNW field was severely limited by the presence of a bright radio source, 3C 244.1 (4.2 Jy at 1.4 GHz), just outside the primary beam. Incomplete subtraction of the time-varying point-spread function response resulted in a strong gradient of additional "noise" across the radio continuum image, with a median value of $1\ \sigma \sim 30\ \mu$Jy in the image center. Therefore, the radio source identification is dependent entirely on the local noise level, and the radio source catalog is complete only at the highest flux density level ($\sim$200 μJy). A more detailed description of these VLA observations will be presented in a later paper (M. S. Yun et al. 2005, in preparation). In this paper we use 387 radio sources brighter than 60 μJy ($\geq$4 σ) in the central $32' \times 32'$ region of the LHEX field and 76 sources in the entire LHNW field.

2.3. *Optical R- and I-Band Imaging*

The *I*-band images of the two Lockman Hole fields were obtained using the 8K CCD camera (Luppino et al. 1996) attached to the f/10 Cassegrain focus of the UH 88 inch (2.2 m) telescope on 1999 May 19–24. This camera has an $18' \times 18'$ field of view. A 2×2 pixel binning was used, yielding a sampling resolution of $0\farcs26$ pixel^{-1}. Nine pointings were used in each field to cover it completely. The total exposure times were 14 and 21 minutes for the LHEX and LHNW fields, respectively. The seeing was about $\sim 0\farcs6$, and the 5 σ detection limit reached $I \sim 22$–23 depending on the location on the camera. Flux calibration was performed using observations of SA 103 and SA 104 (Landolt 1992), with a systematic uncertainty of $\sim$0.05 mag.

The deep *R*-band imaging of both fields was carried out using the prime-focus camera, SuprimeCam (Miyazaki et al. 2002), on the Subaru Telescope on 2001 March 19. This camera has 10 4K $\times$ 2K CCDs, which provides a $34' \times 27'$ field of view with $0\farcs2$ pixel^{-1} sampling. During our observing run, one CCD on the corner of the focal plane was not available. To cover the entire *ISO* survey fields, four different pointings were used in each field. The exposure times were 30 minutes for the two pointings on the west and 25 minutes for the two pointings on the east. The wide-field optical corrector unit of the SuprimeCam introduces significant image distortion on the focal plane (e.g., $18''$ distortion at $20'$ away from the center). This distortion is corrected using the IRAF task *geotran*. The 5 σ detection limit reaches 26.5 mag under a typical seeing of $\sim 0\farcs8$. Flux calibration was performed using observations of the SA 101 (Landolt 1992) and SA 57 (Majewski et al. 1994) fields, with an estimated systematic uncertainty of $\sim$0.08 mag.

The astrometry calibration of all optical images was obtained by comparing with the positions of stars in the USNO-A2.0 catalog (Monet et al. 1998). The astrometric uncertainty is estimated to be less than $1\farcs0$ for both *R*- and *I*-band imaging.

2.4. *Optical Spectroscopy*

We performed spectroscopy of optical objects identified as radio counterparts to the FIR sources. The Keck II telescope at the Mauna Kea Observatory and the WIYN[15] 3.5 m telescope at the

---

[14] The National Radio Astronomy Observatory is a facility of the NSF operated under cooperative agreement by Associated Universities, Inc.

[15] The WIYN Observatory is a joint facility of the University of Wisconsin-Madison, Indiana University, Yale University, and the NOAO.

TABLE 1
RADIO SOURCES WITHIN A 3 σ FIR ERROR CIRCLE

SOURCE	AREA (arcmin^2)	$N_{\rm all}$[a]	N_R[b]	ASSOCIATION N_S[c]	N_M[d]	$\frac{N_S+N_M}{N_{\rm all}}$[e]	IDENTIFICATION[f] $N_{\rm id}$	$N_{\rm id}/N_{\rm all}$
LHEX 90 μm...........	1089	49	387	15	25	0.82	27	0.55
LHEX 170 μm..........	1089	9	387	0	9	1.00	8	0.89
LHNW 90 μm	1552	67	76	17	2	0.28	15	0.22
LHNW 170 μm	1552	11	76	5	2	0.63	5	0.45

NOTE.—The error circle corresponds to a 54″ radius at 90 μm and 90″ at 170 μm.
[a] The number of FIR sources for this study.
[b] The number of radio sources for this study.
[c] The number of FIR sources with a single radio source within its FIR error circle.
[d] The number of FIR sources with multiple radio sources within its FIR error circle.
[e] Fraction of FIR sources with one or more radio counterpart candidates.
[f] Results of the source identification. See § 3.2.

Kitt Peak National Observatory were used with wide wavelength coverage, allowing many emission features for line identification.

2.4.1. *Keck Observations*

Spectroscopic observations with the Keck II telescope were performed preferentially in order of optical brightness on 2000 March 30–31 and on 2001 January 23–24, using the Echelle Spectrograph and Imager (ESI; Sheinis et al. 2000) in low-dispersion mode. The long slit was set to the optical center of the radio sources. The position angle of the slit was adjusted so that the radio sources could be observed simultaneously from 3900 to 11000 Å. The slit width and length were 1″ (6.5 pixels) and 8′, respectively. The spectral resolution ranged from 800 at the blue part to 300 at the red part. The exposure times were between 300 and 5400 s, depending on the optical brightness of the target sources. Standard data reductions were carried out using IRAF. The presence of emission or absorption lines was determined by eye. In this paper we present 15 Keck II spectra of *ISO* FIR galaxies.

2.4.2. *WIYN HYDRA Observations*

Spectroscopic observations were performed with the HYDRA multiobject spectrometer on the WIYN 3.5 m telescope on 2002 February 19 and 2003 February 6–7 using the red cables (2″ diameter), the 316 line mm^{-1} grating with the G5 filter, and the bench camera. The spectra cover the wavelength region 5020–10000 Å with a spectral resolution of 2.64 Å pixel^{-1}.

To cope with the faint spectra typical in fiber-based spectroscopy, beam switching was used to efficiently remove sky emission features such as fringes and time-dependent airglow emission lines, which were heavily blended in some cases. Beam switching requires two different pointings of the telescope. At pointing A, half of the 96 fibers available for HYDRA were centered on the targets, while the others were set to the sky. At pointing B, the roles of the fibers were switched. Beam switching was repeated seven times every 30 minutes, for a total on-source integration time of 210 minutes.

A specialized IRAF package, DOHYDRA (Valdes 1995), was used to perform scattered light removal, spectra extraction, flat-fielding, fiber throughput correction, and wavelength calibration. Sky subtraction and subsequent spectrum co-adding require a careful treatment and are not fully supported by DOHYDRA. We thus developed special IDL routines to handle these tasks. Sky brightness, which is dominated by airglow emission lines, varies with air mass and time. The sky spectra were removed from the "on-target" fibers by using the sky background determined from the preceding and following "sky" fibers. Some scaling of the sky background was required to subtract time-dependent OH airglow emission. After subtracting the sky, the CCD fringes at on-target fibers were reduced greatly. The resulting sky-subtracted spectra were then co-added to improve the signal-to-noise ratio. Extragalactic emission lines were searched for by eye and by comparing the source spectra with the airglow spectra and distinguishing the residual airglow from real emission lines.

Spectra were obtained for a total of 50 objects in the two fields. The brightness of the target objects ranges between $R = 17$ and 21. Nine of the 50 objects are *ISO* FIR sources identified as radio counterparts. The remainder are other faint radio sources identified by the deep radio survey.

3. RADIO COUNTERPART IDENTIFICATION

In this section we illustrate the process of identifying FIR sources with 1.4 GHz radio sources. Our 1.4 GHz survey was carried out within the two *ISO* fields in the Lockman Hole. The areas in which the present identifications were performed were 1089 arcmin^2 in LHEX and 1552 arcmin^2 in LHNW. The typical position uncertainty of the radio sources was $\sim$1″, negligibly smaller than the typical *ISO* FIR position uncertainty.

The original catalogs by Kawara et al. (2004) contain sources with signal-to-noise ratios of 3 σ or better. In the present work we exclude faint sources that have $F^C(90\ \mu{\rm m}) < 43$ mJy or $F^C(170\ \mu{\rm m}) < 102$ mJy, which correspond to the catalog fluxes $F(90\ \mu{\rm m}) < 100$ mJy or $F(170\ \mu{\rm m}) < 200$ mJy, respectively. Accordingly, we adopt position uncertainties of 1 $\sigma_{\rm pos}(90\ \mu{\rm m}) = 18''$ and 1 $\sigma_{\rm pos}(170\ \mu{\rm m}) = 30''$ (see Fig. 4 of Kawara et al. 2004). Excluding UGC 06009, which is the only *IRAS* source within the survey areas and is used for the flux calibration, the total numbers of 90 and 170 μm sources included in this study are 116 and 20, respectively.

Large FIR error circles and a high number density of faint radio sources ensure that there is a high probability of having confusing multiple radio sources within each FIR error circle. For example, 25 out of 49 ($\sim$50%) of the 90 μm sources in the LHEX field have two or more radio sources within a 3 σ error circle (54″ radius; see Table 1). Thus, the task at hand is to reject confusing radio sources that are within the error circle by chance by quantifying the reliability of every identification through a statistical approach as discussed below.

3.1. *Likelihood Ratio Analysis*

Likelihood ratio analysis using cross-association (de Ruiter et al. 1977; Sutherland & Saunders 1992; Mann et al. 1997; Rutledge et al. 2000) is a commonly used technique for identifying

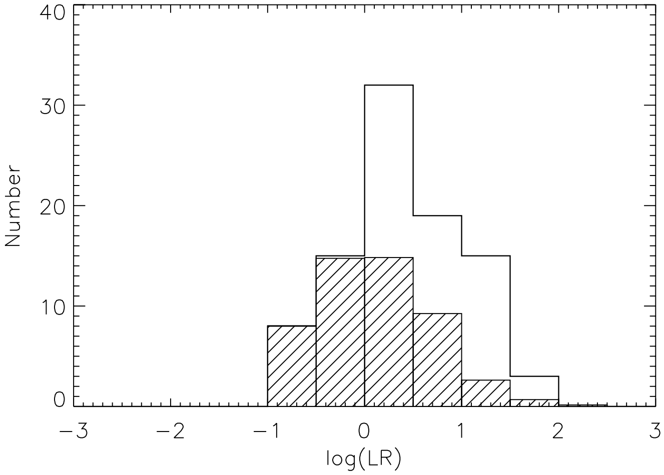

FIG. 2.—Number distributions as a function of LR for radio sources lying within the 3 σ error circle centered at the *ISO* 90 μm source position. The open histogram shows the observed distribution $N_{\rm src}$(LR), while the hatched histogram shows the background distribution obtained from assigning randomly generated positions to the radio sources, $N_{\rm ran}$(LR).

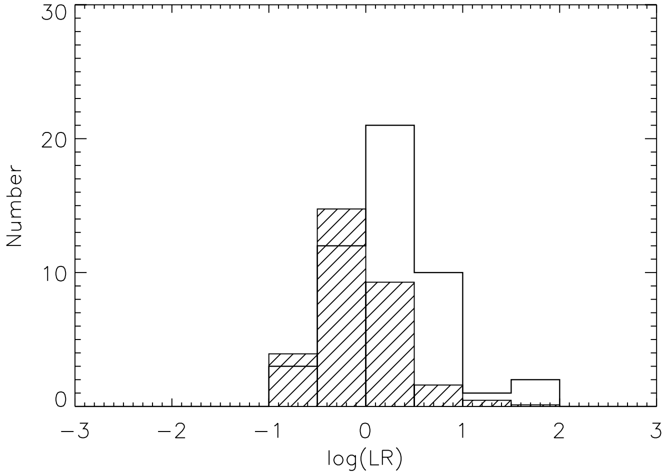

FIG. 3.—Same as Fig. 2, but for the 170 μm sources.

sources in crowded fields. Here we adopt the prescription given by Rutledge et al. (2000). It is assumed that each FIR source is physically associated with either one radio source or none. It is also assumed that there are two types of FIR sources; one type has one real radio counterpart, while the second type has no real radio counterpart. Because of the source confusion due to the high number density of radio sources, in many cases there are one or more radio sources found within a 3 σ error circle centered at the FIR position.

To assess the reliability of individual identifications, we begin with the likelihood ratio described by de Ruiter et al. (1977) and Wolstencroft et al. (1986). The position uncertainty and number density of radio sources are known, and it is assumed that each source has one or more candidate radio counterparts within a 3 σ error circle. A dimensionless angular distance r between the FIR and radio positions is defined as

$$r^2 = \left(\frac{\Delta\theta^2}{\sigma_{\rm pos}^2 + \sigma_R^2} \right), \tag{3}$$

where $\Delta\theta$ is the positional difference between the FIR and radio sources and σ_R is the standard deviation of the radio positions. As already discussed, σ_R is typically $\sim 1''$ and negligible when compared with FIR error, $\sigma_{\rm pos} \sim 18''$ or $30''$. Thus, we adopt $r = \Delta\theta/\sigma_{\rm pos}$. The surface density of radio sources, $n(f)$, is the number density of radio sources with 1.4 GHz flux equal to or greater than f, and it is adopted from Richards (2000).

Assuming that a FIR source and its *true* radio counterpart are located at the same position, the measured separation r is due to the FIR position uncertainty. Then, the probability $dp_{\rm id}$ of having a real radio counterpart at a distance between r and $r + dr$ from the FIR source is $dp_{\rm id} = r \exp(-r^2/2)\, dr$. The probability dp_c of finding one confusing object between r and $r + dr$ from the FIR source is a product of two probabilities: the probability of not having a counterpart within r, which is given by $e^{-\pi r^2 \sigma^2 n(f)}$, and the probability of having a confusing object between r and $r + dr$, which is

$$1 - e^{-2\pi r dr \sigma^2 n(f)} \sim 2\pi r \sigma^2 n(f)\, dr.$$

Thus, the probability dp_c is expressed as

$$dp_c = \left[2\pi\sigma^2 n(f) r\, dr\right] \exp\left[-\pi r^2 \sigma^2 n(f)\right].$$

The likelihood ratio is defined as the ratio $dp_{\rm id}/dp_c$:

$$\mathrm{LR}(r, f) = \frac{1}{2\pi\sigma^2 n(f)} \exp\left[-\frac{r^2}{2} + \pi r^2 \sigma^2 n(f)\right]. \tag{4}$$

For each FIR source, LR is calculated for all radio sources within the 3 σ error circle. Then the frequency distribution N(LR) is computed. Figures 2 and 3 show the distribution of LR as open histograms for 90 and 170 μm. The LR distribution was derived only in the LHEX field, because the LHNW field radio data suffered from nonuniform noise and complex source statistics.

Once the distribution of the likelihood ratio LR is determined, a reliability R for identification with LR can be quantified as

$$R(\mathrm{LR}) = \frac{N_{\rm true}(\mathrm{LR})}{N_{\rm true}(\mathrm{LR}) + N_{\rm false}(\mathrm{LR})}, \tag{5}$$

where $N_{\rm true}$(LR) and $N_{\rm false}$(LR) are the numbers of true and false radio counterparts, respectively. In practice, however, it is

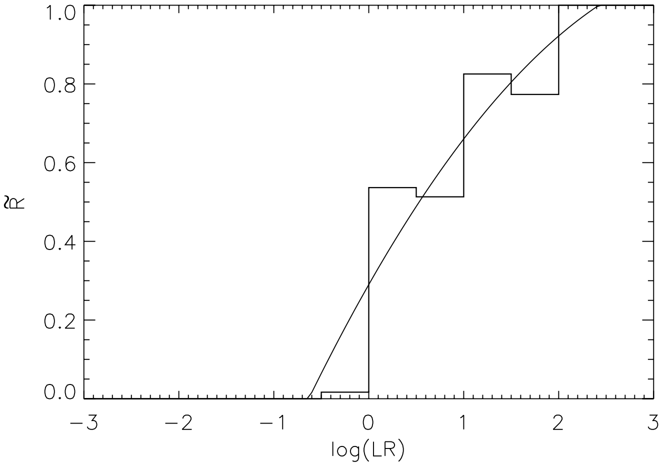

FIG. 4.—Modified reliability $\tilde{R}$ as a function of LR for the 90 μm sources. The solid line is a fit to $\tilde{R}$: $\tilde{R} = 0.29 + 0.42x - 0.05x^2$, where $x = \log(\mathrm{LR})$. This function is used as an input for deriving the probability for source identification $P_{{\rm id},i}$ and no identification $P_{\rm no\text{-}id}$.

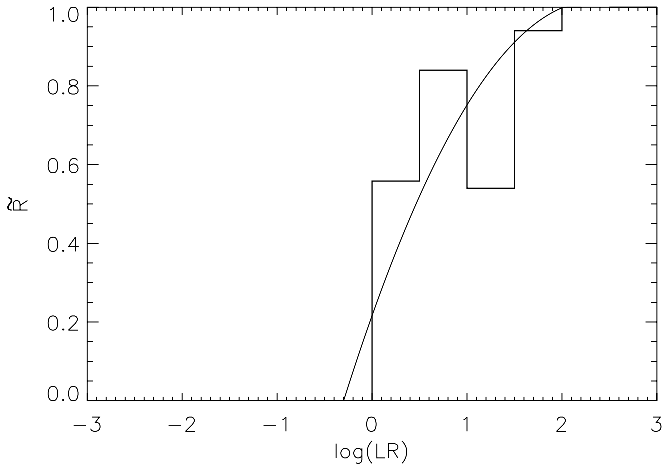

FIG. 5.—Same as Fig. 4, but for the 170 μm sources. The solid curve is $\tilde{R} = 0.21 + 0.68x - 0.14x^2$, where $x = \log(\mathrm{LR})$.

generally unknown which radio source is the real counterpart or what N_{true} and N_{false} are.

The denominator in equation (5) can be rewritten as

$$N_{\mathrm{true}}(\mathrm{LR}) + N_{\mathrm{false}}(\mathrm{LR}) = N_{\mathrm{src}}(\mathrm{LR}), \tag{6}$$

where $N_{\mathrm{src}}(\mathrm{LR})$ is the total number of radio sources with LR in the field. In general N_{true} is not known, but we can estimate N_{true} from the difference between N_{src} and N_{ran}, where N_{src} and N_{ran} are the numbers of radio sources in regions containing FIR sources and containing no FIR sources, respectively. There is not enough area free from *ISO* FIR sources because of the high source density and large positional uncertainty of the *ISO* FIR sources. We estimate $N_{\mathrm{ran}}(\mathrm{LR})$ by randomly assigning positions to radio sources in the catalog. These simulations are repeated 100 times and averaged. The resulting $N_{\mathrm{ran}}(\mathrm{LR})$ is shown as hatched histograms in Figures 2 and 3. Comparing the observed distributions $N_{\mathrm{src}}(\mathrm{LR})$ with the randomly generated $N_{\mathrm{ran}}(\mathrm{LR})$, it is clear that $N_{\mathrm{src}}(\mathrm{LR})$ exceeds $N_{\mathrm{ran}}(\mathrm{LR})$ for $\log(\mathrm{LR}) \gtrsim 0$.

Our radio catalog consists of both kinds of radio sources: "real" and "false" counterparts of FIR sources. Thus, $N_{\mathrm{ran}}(\mathrm{LR})$ should be greater than $N_{\mathrm{false}}(\mathrm{LR})$. Using $N_{\mathrm{ran}}(\mathrm{LR})$, $N_{\mathrm{true}}(\mathrm{LR})$ is represented as

$$N_{\mathrm{true}}(\mathrm{LR}) \geq N_{\mathrm{src}}(\mathrm{LR}) - N_{\mathrm{ran}}(\mathrm{LR}). \tag{7}$$

Here we introduce the modified reliability $\tilde{R}(\mathrm{LR})$, as defined by

$$\tilde{R}(\mathrm{LR}) = \frac{N_{\mathrm{src}}(\mathrm{LR}) - N_{\mathrm{ran}}(\mathrm{LR})}{N_{\mathrm{src}}(\mathrm{LR})} \leq \frac{N_{\mathrm{true}}(\mathrm{LR})}{N_{\mathrm{src}}(\mathrm{LR})} = R(\mathrm{LR}), \tag{8}$$

where $\tilde{R}$ is plotted in Figures 4 and 5 together with quadratic approximations of $\tilde{R}$ as a function of $\log(\mathrm{LR})$.

As seen in equation (8), $\tilde{R}(\mathrm{LR})$ is less than the true reliability $R(\mathrm{LR})$. The typical ratio $R/\tilde{R}$ for $\log(\mathrm{LR}) > 0$ can be estimated as follows: According to Table 1, the number of radio sources is 387, and 27 of them are identified with 90 μm sources. Thus, the fraction of true radio counterparts is 27/387. Because of randomly assigned radio positions in the simulation, this fraction should be independent of LR. In Figure 2 $N_{\mathrm{src}}(\log(\mathrm{LR}) > 0) = 69$ and $N_{\mathrm{ran}}(\log(\mathrm{LR}) > 0) = 28$. Then, $N_{\mathrm{false}}(\log(\mathrm{LR}) > 0)$ is $28(1 - 27/387)$. Substituting these into equations (5) and (8),

$$R = [69 - 28(1 - 27/387)]/69 = 0.62,$$

and $\tilde{R} = (69 - 28)/69 = 0.59$. Thus, $R(\mathrm{LR})/\tilde{R}(\mathrm{LR}) = 1.05$ for $\log(\mathrm{LR}) > 0$, and the difference between the true and modified reliability, R and $\tilde{R}$, is small.

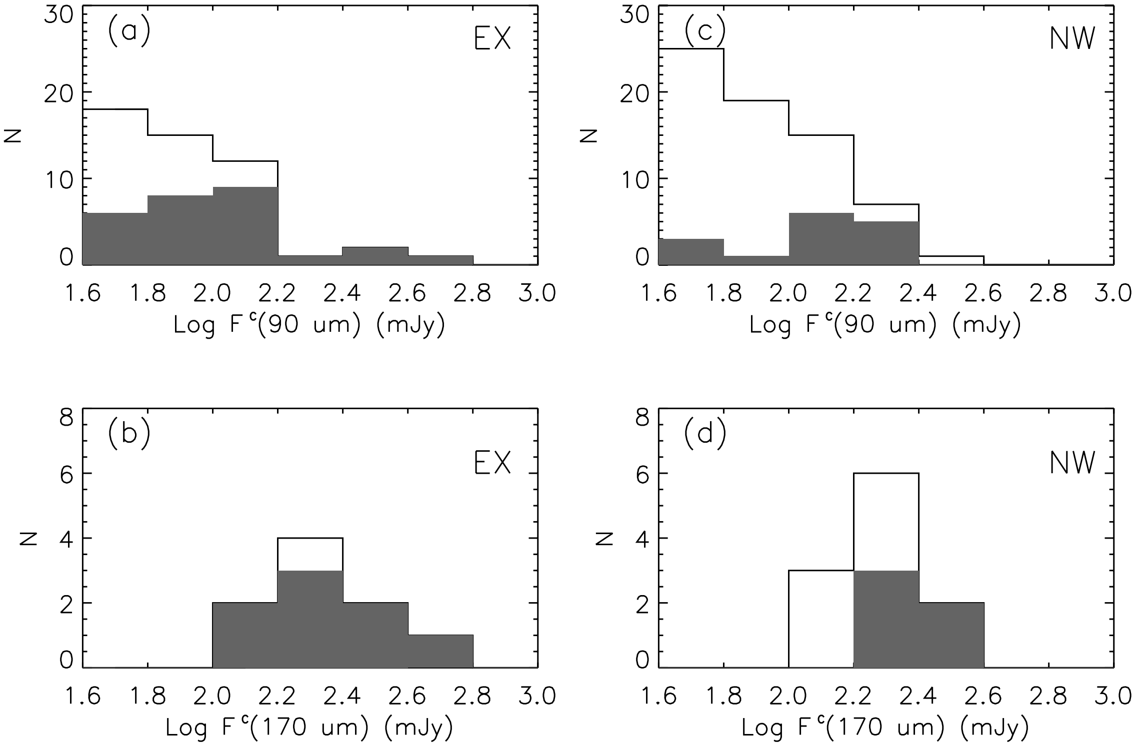

FIG. 6.—Histograms of FIR sources. The open histograms show the distributions of all FIR sources used for the identification analysis, while the filled histograms represent the distribution of identified FIR sources. (*a*) For 90 μm sources in the LHEX field; (*b*) for 170 μm sources in LHEX; (*c*) for 90 μm sources in LHNW; and (*d*) for 170 μm sources in LHNW.

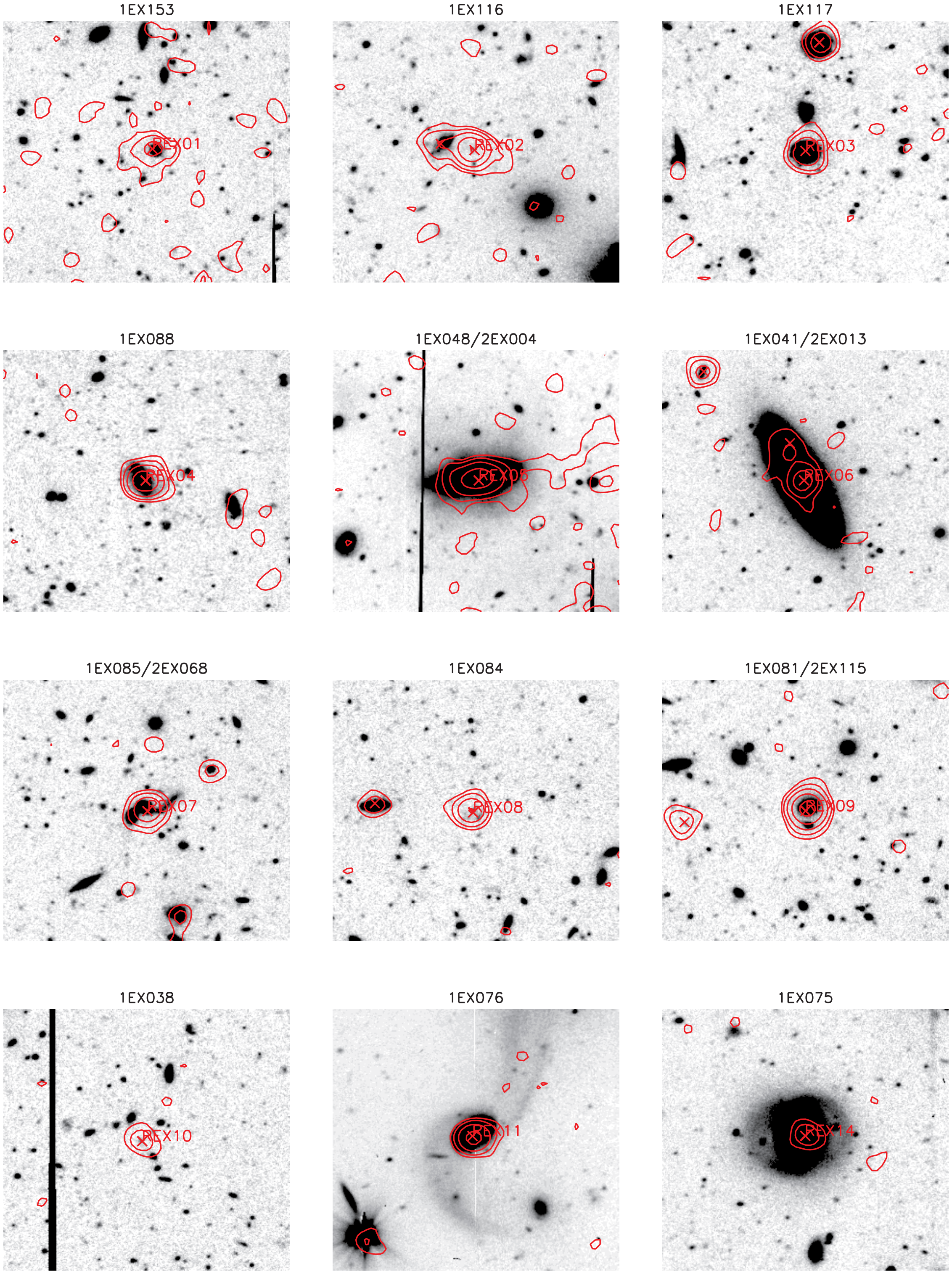

FIG. 7.—*R*-band images centered at the positions of the radio counterparts. The image sizes are $60'' \times 60''$. North is up, and east is to the left. Red 1.4 GHz contours are plotted at steps of 2, 4, 8, 16, and 32 σ. Crosses present the positions of the 1.4 GHz radio sources.

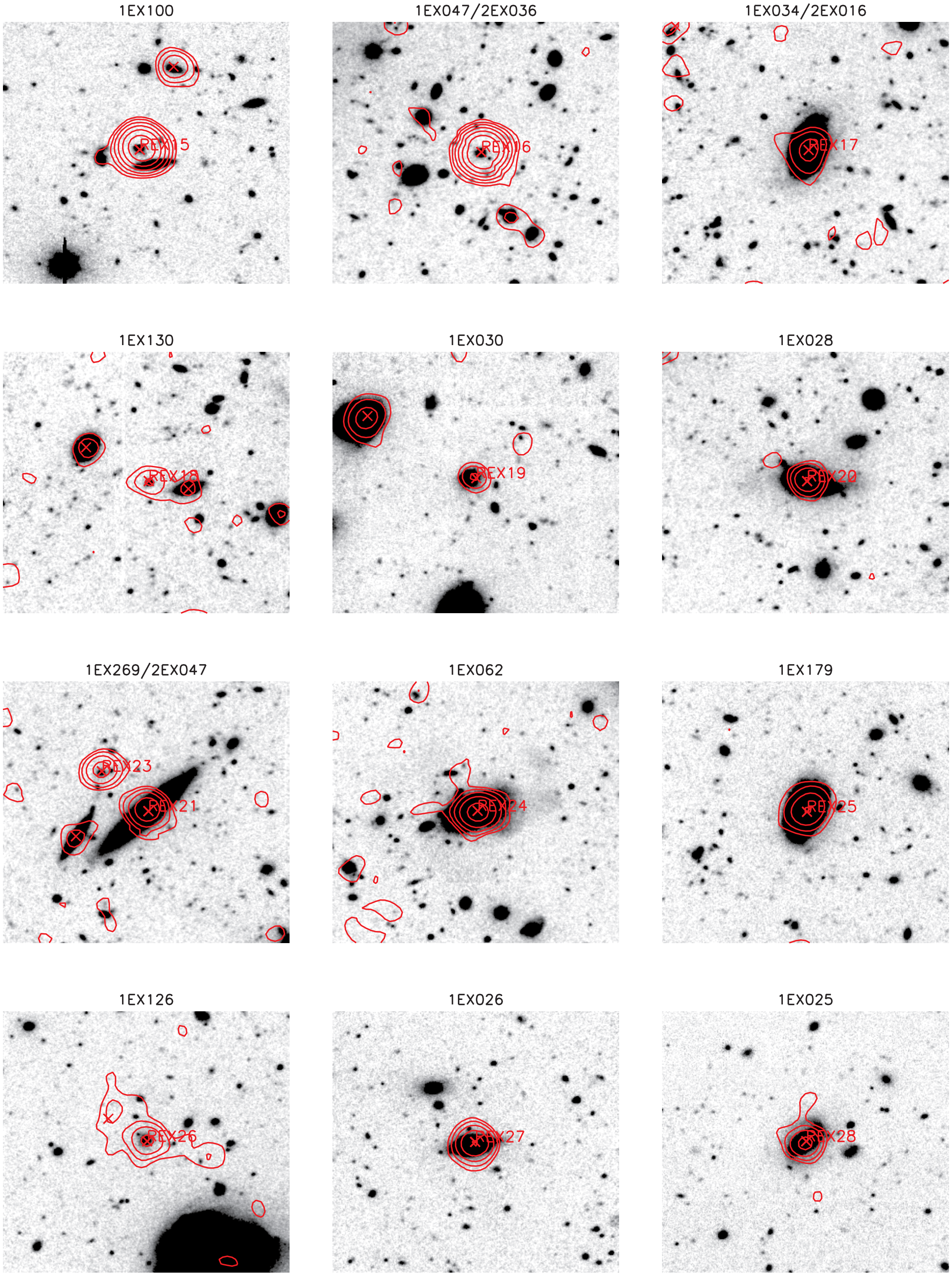

FIG. 7.—*Continued*

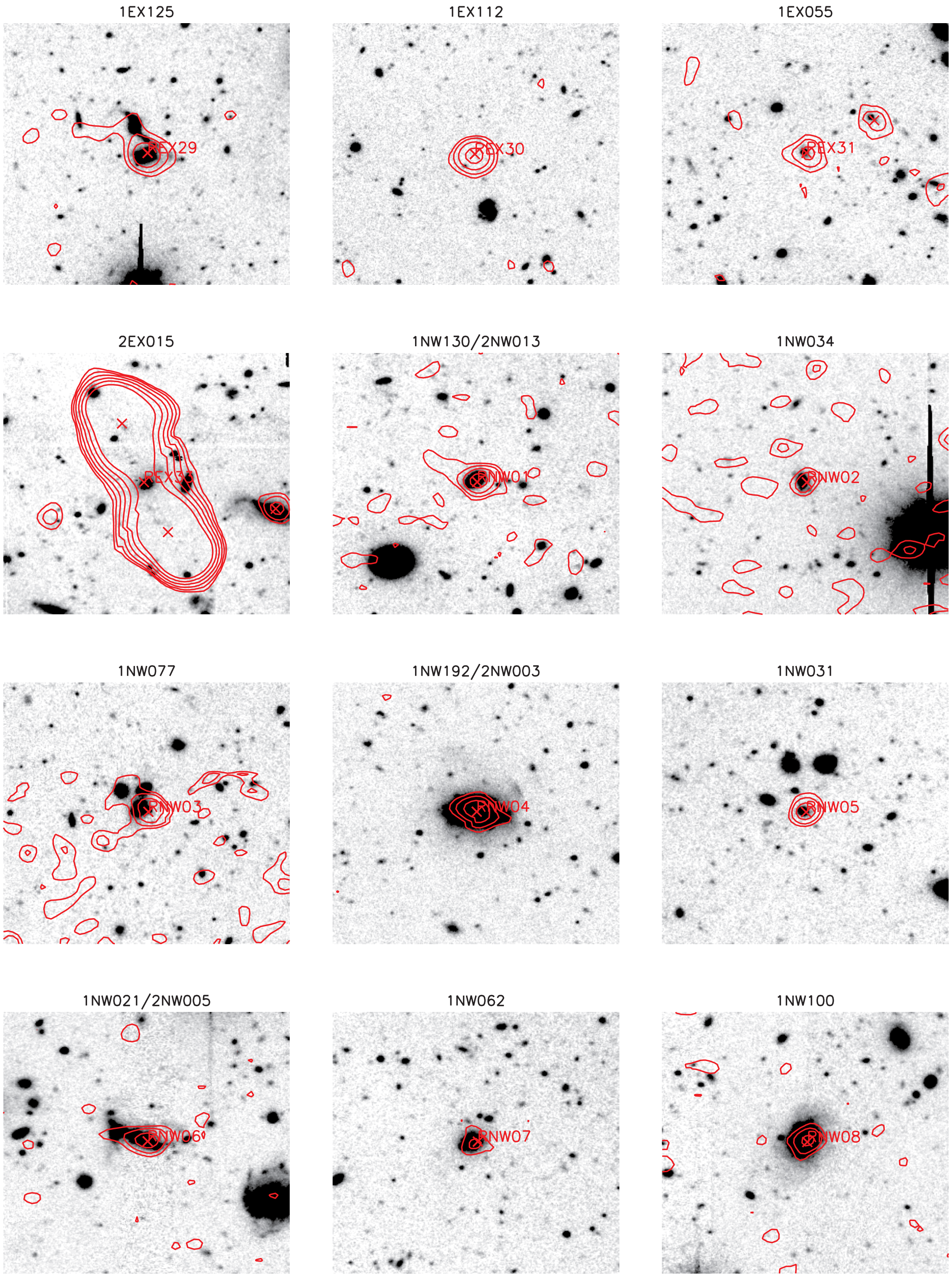

Fig. 7.—*Continued*

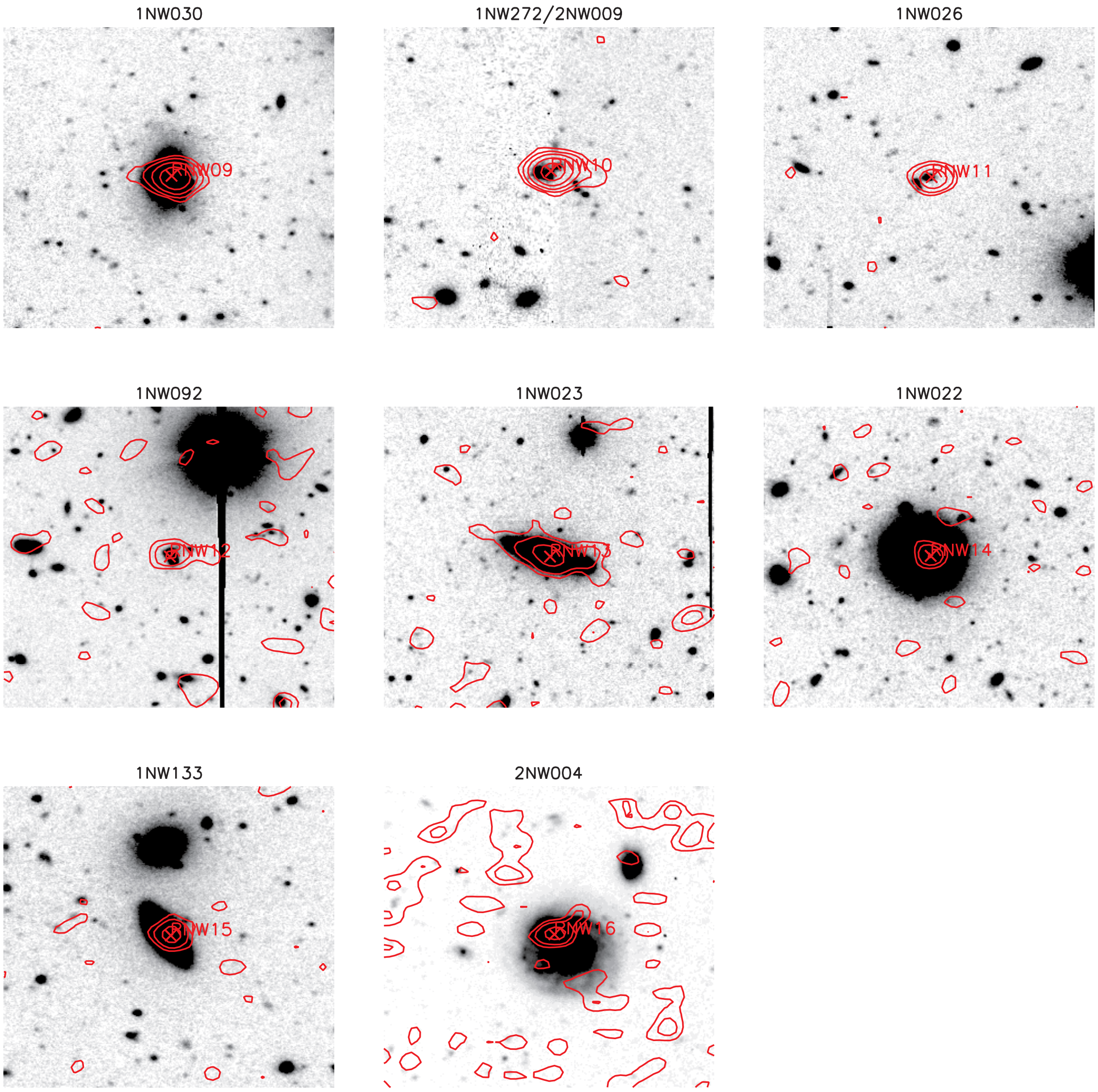

FIG. 7.—*Continued*

Where more than one radio source is found within a 3 σ error radius, the sum of R of the individual sources frequently exceeds unity. Thus, it is necessary to normalize R so that the sum of R plus the probability of having no radio counterpart is unity. Suppose that there are M radio candidates, one or none of which is a true radio counterpart. Also, $P_{\mathrm{id},i}$ and $P_{\text{no-id}}$ denote the probability that the ith candidate is the uniquely true radio counterpart and that none of the radio candidates is the real radio counterpart, respectively. Then, the probability of the ith candidate being true and false is $\tilde{R}_i$ and $(1-\tilde{R}_i)$, respectively. Thus, $P_{\text{no-id}}$ and $P_{\mathrm{id},i}$ are

$$P_{\text{no-id}} = \frac{\Pi_{j=1}^{M}\left(1-\tilde{R}_j\right)}{S}, \tag{9}$$

$$P_{\mathrm{id},i} = \frac{\tilde{R}_i \Pi_{j\neq i}^{M}\left(1-\tilde{R}_j\right)}{S}, \tag{10}$$

where S is a normalization factor specific to each *ISO* FIR source. Setting the sum of all the probabilities to unity gives

$$P_{\text{no-id}} + \sum_{i=1}^{M} P_{\mathrm{id},i} = 1. \tag{11}$$

The normalization factor S is derived as

$$S = \sum_{i=1}^{M} \tilde{R}_i \Pi_{j\neq i}^{M}\left(1-\tilde{R}_j\right) + \Pi_{j=1}^{M}\left(1-\tilde{R}_j\right). \tag{12}$$

3.2. *Identification*

The main criterion adopted for a true radio counterpart identification is the condition $P_{\mathrm{id}} > P_{\text{no-id}}$. The results are summarized in Table 1. In the LHEX field, 27 of 49 90 μm sources are identified with radio sources. The identification rate is higher in bright sources than in fainter sources, as shown in Figure 6. The rate is 81% (13/16) for 90 μm sources brighter than 100 mJy, while it is reduced to 42% (14/33) for sources fainter than 100 mJy. This is due to poorer positional accuracy (Kawara et al. 2004) for fainter sources. Seven of nine 170 μm sources in the LHEX field meet our criterion. Five of them have the same identification as their 90 μm counterpart. One exception is 1EX085/2EX068, for which the 90 μm identification is given priority for the reason described at the end of this section. While one additional source, 2EX016, does not meet our identification criterion, the identified radio source for the associated 90 μm source, 1EX034, is regarded as

TABLE 2

List of the Identified Far-Infrared Sources at 90 μm

Name													
C_90 (1)	C_160^a (2)	1.4 GHz (3)	R.A.^{b} (4)	Decl.^{b} (5)	F^C(90 μm)^c (mJy) (6)	F^C(170 μm)^c (mJy) (7)	F(1.4 GHz) (μJy) (8)	R (9)	I (10)	Dist. (arcsec) (11)	LR (12)	P_{id} (13)	$P_{no\text{-}id}$ (14)
LHEX													
1EX153	. . .	REX01	10 50 02.13	+57 16 21.3	56 ± 16	. . .	143	21.8	21.5	13	6.88	0.48	0.31
1EX116	. . .	REX02	10 50 12.54	+57 11 36.8	107 ± 12	. . .	377	24.1	>22.0	34	4.41	0.41	0.35
1EX117	. . .	REX03	10 50 19.73	+57 28 13.2	66 ± 12	. . .	227	19.1	18.5	16	9.99	0.43	0.22
1EX088	. . .	REX04	10 50 37.55	+57 28 44.9	104 ± 23	. . .	392	19.8	19.0	9	21.48	0.67	0.21
1EX048	2EX004	REX05	10 50 41.99	+57 07 06.4	254 ± 19	407 ± 30	346	16.3	15.8	12	17.15	0.67	0.25
1EX041	2EX013	REX06	10 50 52.39	+57 35 07.5	310 ± 80	343 ± 88	182	<15.3^d	14.7	9	10.01	0.42	0.22
1EX085	2EX068	REX07	10 50 56.57	+57 16 31.2	73 ± 24	125 ± 14	242	20.5	19.8	14	11.53	0.54	0.26
1EX084	. . .	REX08	10 51 00.90	+57 20 36.0	114 ± 21	. . .	261	24.3	22.0	17	10.69	0.57	0.28
1EX081	2EX115	REX09	10 51 13.44	+57 14 26.2	88 ± 16	212 ± 47	611	20.0	19.1	5	34.36	0.72	0.16
1EX038	. . .	REX10	10 51 19.66	+57 28 04.0	43 ± 13	. . .	94	24.5	>22.0	18	3.65	0.51	0.49
1EX076	. . .	REX11	10 51 28.07	+57 35 02.4	152 ± 17	. . .	303	16.6	16.3	18	11.53	0.34	0.16
		REX12	10 51 20.86	+57 35 32.6			7177	24.9	>22.0	47	7.99	0.27	0.16
		REX13	10 51 25.68	+57 35 44.2			497	15.5	15.2	32	6.59	0.24	0.16
1EX075	. . .	REX14	10 51 34.41	+57 33 59.9	53 ± 18	. . .	110	16.6	16.0	21	3.72	0.41	0.39
1EX100	. . .	REX15	10 51 37.01	+57 29 40.8	54 ± 14	. . .	1901	22.3	21.7	34	15.00	0.57	0.23
1EX047	2EX036	REX16	10 51 52.38	+57 09 50.1	113 ± 21	252 ± 46	2642	22.2	21.2	23	50.76	0.76	0.13
1EX034	2EX016	REX17	10 52 07.19	+57 07 44.8	124 ± 18	184 ± 27	159	17.1	16.5	7	9.13	0.60	0.33
1EX130	. . .	REX18	10 52 31.82	+57 09 27.1	54 ± 12	. . .	123	22.9	21.7	17	5.07	0.31	0.24
1EX030	. . .	REX19	10 52 39.55	+57 24 31.0	132 ± 29	. . .	136	17.7	17.6	5	8.01	0.46	0.27
1EX028	. . .	REX20	10 52 52.76	+57 07 53.7	150 ± 33	. . .	260	17.5	16.8	32	3.80	0.52	0.48
1EX269	2EX047	REX21	10 52 56.82	+57 08 25.7	206 ± 53	163 ± 42	439	16.8	16.2	22	13.29	0.39	0.17
		REX22	10 52 52.76	+57 07 53.7			260	17.5	16.8	30	4.55	0.20	0.17
		REX23	10 52 58.00	+57 08 34.8			337	22.7	21.0	34	3.94	0.18	0.17
1EX062	. . .	REX24	10 53 01.36	+57 05 42.9	399 ± 29	. . .	705	16.9	16.3	4	39.33	0.83	0.17
1EX179	. . .	REX25	10 53 18.96	+57 21 40.4	129 ± 29	. . .	247	17.1	16.6	7	14.48	0.60	0.25
1EX126	. . .	REX26	10 53 22.83	+57 15 00.0	74 ± 16	. . .	261	21.4	20.2	5	15.77	0.57	0.22
1EX026	. . .	REX27	10 53 25.30	+57 29 11.4	90 ± 20	. . .	507	17.6	17.4	8	27.18	0.76	0.21
1EX025	. . .	REX28	10 53 28.01	+57 11 15.5	67 ± 15	. . .	300	18.2	17.6	10	15.91	0.72	0.28
1EX125	. . .	REX29	10 53 26.68	+57 14 05.9	83 ± 12	. . .	226	19.3	18.7	15	10.25	0.66	0.34
1EX112	. . .	REX30	10 53 42.08^e	+57 30 26.1^e	74 ± 25	. . .	335	24.6	>22.0	18	13.05	0.70	0.30
1EX055	. . .	REX31	10 53 57.76	+57 23 47.1	61 ± 20	. . .	119	22.5	21.3	18	4.59	0.37	0.31
LHNW													
1NW130	2NW013	RNW01	10 31 23.03	+57 42 26.4	172 ± 19	359 ± 53	677	20.0	19.1	10	32.89	0.81	0.19
1NW034	. . .	RNW02	10 31 47.58	+57 49 27.5	119 ± 22	. . .	200	20.5	19.7	24	5.58	0.58	0.42
1NW077	. . .	RNW03	10 32 05.80	+58 02 39.2	122 ± 22	. . .	447	20.2	19.0	9	24.22	0.77	0.23
1NW192	2NW003	RNW04	10 32 49.52	+57 37 07.9	226 ± 33	262 ± 39	420	17.1	16.5	9	22.94	0.77	0.23
1NW031	. . .	RNW05	10 33 15.43	+57 31 01.8	128 ± 28	. . .	408	21.6	20.6	34	4.50	0.54	0.46
1NW021	2NW005	RNW06	10 33 20.20	+57 49 13.1	127 ± 23	192 ± 50	343	18.7	18.0	11	17.71	0.74	0.26
1NW062	. . .	RNW07	10 33 30.28	+57 42 25.0	57 ± 15	. . .	143	19.9	19.1	15	6.48	0.60	0.40
1NW100	. . .	RNW08	10 33 52.36	+57 27 01.4	62 ± 9	. . .	292	17.7	17.3	19	10.62	0.67	0.33
1NW030	. . .	RNW09	10 33 58.71	+57 43 17.3	105 ± 19	. . .	915	17.3	16.6	11	41.41	0.83	0.17
1NW272	2NW009	RNW10	10 33 59.09	+57 29 52.4	91 ± 20	199 ± 29	1493	20.8	19.1	15	53.34	0.86	0.14
1NW026	. . .	RNW11	10 35 13.69	+57 34 44.6	51 ± 13	. . .	434	21.9	21.0	9	23.56	0.77	0.23
1NW092	. . .	RNW12	10 36 04.05	+57 48 12.2	205 ± 38	. . .	267	19.5	18.9	20	9.41	0.65	0.35
1NW023	. . .	RNW13	10 36 06.52	+57 47 02.1	169 ± 31	. . .	670	16.7	16.2	23	17.69	0.72	0.26
1NW022	. . .	RNW14	10 36 11.61	+57 43 21.1	101 ± 22	. . .	262	16.3	15.6	3	16.19	0.72	0.28
1NW133	. . .	RNW15	10 36 15.41	+57 39 14.7	169 ± 37	. . .	338	16.8	16.1	13	16.31	0.72	0.28

Note.—Units of right ascension are hours, minutes, and seconds, and units of declination are degrees, arcminutes, and arcseconds.

[a] The positional association of FIR sources in both bands comes from Kawara et al. (2004).

[b] The J2000.0 coordinates come from the VLA 1.4 GHz radio data.

[c] This is the bias-corrected flux density using eq. (1).

[d] R-band photometry is not available due to saturation.

[e] The positional difference between the optical and radio is 3.″0, which is larger than the typical error of 0.″6.

TABLE 3

List of the Identified Far-Infrared Sources at 170 μm

Name													
C_160 (1)	C_90[a] (2)	1.4 GHz (3)	R.A.[b] (4)	Decl.[b] (5)	F^C(170 μm)[c] (mJy) (6)	F^C(90 μm)[c] (mJy) (7)	F(1.4 GHz) (μJy) (8)	R (9)	I (10)	Dist. (arcsec) (11)	LR (12)	P_{id} (13)	$P_{no\text{-}id}$ (14)
						LHEX							
2EX004	1EX048	REX05	10 50 41.99	+57 07 06.4	407 ± 30	254 ± 19	346	16.3	15.8	16	6.79	0.51	0.25
2EX013	1EX041	REX06	10 50 52.39	+57 35 07.5	343 ± 88	310 ± 80	182	15.3	14.7	22	3.34	0.39	0.35
2EX068	1EX085	REX32	10 50 56.54	+57 15 32.7	125 ± 14	73 ± 24	462	22.8	22.3	27	7.03	0.45	0.21
		REX07	10 50 56.57	+57 16 31.2		. . .	242	20.5	19.8	34	3.19	0.22	0.21
2EX115	1EX081	REX09	10 51 13.44	+57 14 26.2	212 ± 47	88 ± 16	611	20.0	19.1	40	5.74	0.50	0.28
2EX036	1EX047	REX16	10 51 52.38	+57 09 50.1	252 ± 46	113 ± 21	2642	22.2	21.2	37	19.85	0.77	0.14
2EX016	1EX034	REX17	10 52 07.19	+57 07 44.8	184 ± 27	124 ± 18	159	17.1	16.5	32	2.36	0.30[d]	0.39[d]
2EX015	. . .	REX33	10 52 37.38[e]	+57 31 03.5[e]	151 ± 38	. . .	14667	20.7	19.1	33	82.74	0.96	0.01
2EX047	1EX269	REX21	10 52 56.82	+57 08 25.7	163 ± 42	206 ± 53	439	16.8	16.2	29	6.25	0.33	0.18
		REX22	10 52 52.76	+57 07 53.7		. . .	260	17.5	16.8	28	4.11	0.23	0.18
		REX23	10 52 58.00	+57 08 34.8		. . .	337	22.7	21.0	41	3.37	0.19	0.18
						LHNW							
2NW013	1NW130	RNW01	10 31 23.03	+57 42 26.4	359 ± 53	172 ± 19	677	20.0	19.1	19	11.50	0.76	0.24
2NW003	1NW192	RNW04	10 32 49.52	+57 37 07.9	262 ± 39	226 ± 33	420	17.1	16.5	27	6.43	0.66	0.34
2NW005	1NW021	RNW06	10 33 20.20	+57 49 13.1	192 ± 50	127 ± 23	343	18.7	18.0	13	6.99	0.62	0.30
2NW004	. . .	RNW16	10 33 41.32	+58 02 21.1	165 ± 41	. . .	380	18.0	17.2	26	6.00	0.65	0.35
2NW009	1NW272	RNW10	10 33 59.09	+57 29 52.4	199 ± 29	91 ± 20	1493	20.8	19.1	31	16.01	0.82	0.18

[a] The positional association of FIR sources in both bands comes from Kawara et al. (2004).

[b] The J2000.0 coordinates come from the VLA 1.4 GHz radio data.

[c] This is the bias-corrected flux density using eq. (2).

[d] The radio source of 2EX016 does not meet our criterion, $P_{id} > P_{no\text{-}id}$. However, the associated 90 μm source, 1EX034, is identified with a radio source, which is regarded as the counterpart of 1EX034/2EX016.

[e] The position comes from the optical image because the associated radio source position is dominated by the bright, extended radio lobes.

the true counterpart. In summary, a total of eight 170 μm sources are identified.

Because of the higher effective noise in the radio continuum image of the LHNW field, there are only a few cases in which two or more radio candidates are found. To proceed with the same source identification criterion, the reliability functions derived from the LHEX field were applied to the LHNW field as well. As a result, 15 of 67 sources and 5 of 11 sources in 90 μm and 170 μm are identified with radio sources. The identification rate is 48% (11/23) for 90 μm sources brighter than 100 mJy and 9% (4/44) for sources fainter than 100 mJy.

Optical identification was made by searching for optical objects within a $2''$ radius of the radio counterpart on the Subaru R-band image. If no objects were found, bright objects ($R < 20$) were searched for within a $5''$ radius from the radio counterpart. All the radio counterparts were identified with an optical object. The dispersion of separation between radio and optical sources was only $0''.6$. All the optical counterparts were galaxies except for 1EX030, which is a pointlike source showing broad emission lines characteristic of a quasar. The R-band images are shown together with 1.4 GHz contours in Figure 7.

Individual radio counterparts are listed together with the optical data in Tables 2 and 3 for the 90 and 170 μm sources. In columns (1) and (2), names of the 90 and 170 μm sources are given. In column (3), the names of radio sources are given in order of appearance. In columns (4) and (5), the radio coordinates are given in the J2000.0 system. In columns (6) and (7), the FIR fluxes are given, including the correction for the bias effect (eqs. [1] and [2]). In column (8), the 1.4 GHz flux is given in microjanskys. In columns (9) and (10), the R- and I-band magnitudes are given in the Vega system. Column (11) lists the angular distance of the radio counterpart from the position of the FIR source in arcseconds. In columns (12)–(14), LR, P_{id}, and $P_{no\text{-}id}$ are given. If more than one radio source meets the identification criterion $P_{id} > P_{no\text{-}id}$, then all the radio sources are listed in the tables. Table 4 summarizes the optical and radio properties of the identified *ISO* FIR sources. Source identification is complicated in several cases, and additional details are discussed below.

1EX076: 1EX076 has three radio candidates: two bright galaxies (REX11 and REX13) and one bright radio source (REX12). REX11, REX12, and REX13 are shown in the R-band image in Figure 8*a*. REX11 and REX13 are an interacting galaxy pair at the same redshift of $z = 0.073$. Moreover, REX11 is the closest to 1EX076, and its reliability is the highest among the three objects. REX11 is thus the most likely optical counterpart of this FIR source, although there might also be a significant contribution from REX13.

1EX034/2EX016: Although 2EX016 does not have any radio candidate that meets our identification criterion, 1EX034 is identified with a radio source. This radio source is thus regarded as the counterpart of 1EX034/2EX036.

1EX269/2EX047: As shown in Figure 8*b*, 1EX269 and 2EX047 have three common candidates (REX21, REX22, and REX23). REX21 is regarded as the counterpart because it has the highest reliability among the three.

1EX085/2EX068: 2EX068 has two radio candidates (REX07 and REX32) meeting the criterion, while 1EX085 has only one candidate (REX07) meeting the identification criterion (Fig. 8*c*). Thus, 2EX068 is identified with REX07.

1NW025/2NW006: 1NW025 [$F^C(90\ \mu\text{m}) = 91$ mJy; R.A. $= 10^{h}35^{m}16^{s}.2$, decl. $= +57^{\circ}33'19''$ (J2000.0)] does not have any

TABLE 4

List of Identified FIR Sources

Name		F^C(90 μm) (mJy)	F^C(170 μm) (mJy)	$\frac{L(1.4\ \mathrm{GHz})}{L(90\ \mu\mathrm{m})}$ (10^{-7})	$\frac{L(90\ \mu\mathrm{m})}{L(R)}$	z[a]	log ($L_{\mathrm{FIR}}/L_{\odot}$)	Nature[b]
C_90	C_160							
1EX153	. . .	56	. . .	11.5	69.2	. . .	. . .	. . .
1EX116	. . .	107	. . .	16.0	1063.3	. . .	. . .	. . .
1EX117	. . .	66	. . .	15.6	6.4	. . .	. . .	. . .
1EX088	. . .	104	. . .	17.0	20.3	0.363K	11.7	. . .
1EX048	2EX004	254	407	6.1	2.0	0.091K	10.9	. . .
1EX041	2EX013	310	343	2.6	<0.9	0.028K	9.8	. . .
1EX085	2EX068	73	125	15.0	26.3	0.396K	11.7	i
1EX084	. . .	114	. . .	10.3	1360.4	. . .	. . .	. . .
1EX081	2EX115	88	212	31.1	20.2	0.362K	11.8	. . .
1EX038	. . .	43	. . .	9.8	626.1	. . .	. . .	. . .
1EX076	. . .	152	. . .	9.0	1.5	0.073H	10.3	i, HII
1EX075	. . .	53	. . .	9.2	0.5	0.074H	10.1	. . .
1EX100	. . .	54	. . .	157.9	106.9	. . .	. . .	AGN
1EX047	2EX036	113	252	105.0	200.2	. . .	. . .	AGN
1EX034	2EX016	124	184	5.8	2.0	0.123K	10.8	. . .
1EX130	. . .	54	. . .	10.3	187.1	. . .	. . .	. . .
1EX030	. . .	132	. . .	4.6	3.8	1.110H	13.1	Quasar
1EX028	. . .	150	. . .	7.8	3.4	0.163K	11.0	. . .
1EX269	2EX047	206	163	9.6	2.6	0.080K	10.5	. . .
1EX062	. . .	399	. . .	7.9	5.3	0.080K	10.8	. . .
1EX179	. . .	129	. . .	8.6	2.2	0.133H	10.8	. . .
1EX126	. . .	74	. . .	15.9	61.3	. . .	. . .	. . .
1EX026	. . .	90	. . .	25.3	2.4	0.029H	9.3	HII
1EX025	. . .	67	. . .	20.3	3.0	0.162H	10.8	i, AGN
1EX125	. . .	83	. . .	12.2	10.6	0.231H	11.2	. . .
1EX112[c]	. . .	74	. . .	20.3	1156.1	. . .	. . .	. . .
1EX055	. . .	61	. . .	8.8	145.1	. . .	. . .	. . .
. . .	2EX015	. . .	151	>1527.9	<19.2	0.710K	12.3	AGN
1NW130	2NW013	172	359	17.7	40.0	0.502K	12.4	. . .
1NW034	. . .	119	. . .	7.5	45.7	. . .	. . .	. . .
1NW077	. . .	122	. . .	16.5	32.8	. . .	. . .	i?
1NW192	2NW003	226	262	8.4	3.6	0.115K	11.0	. . .
1NW031	. . .	128	. . .	14.3	125.6	. . .	. . .	. . .
1NW021	2NW005	127	192	12.2	8.7	0.240K	11.5	i
1NW062	. . .	57	. . .	11.3	12.3	0.498B	11.9	. . .
1NW100	. . .	62	. . .	21.3	1.7	0.182B	10.9	. . .
1NW030	. . .	105	. . .	39.3	2.0	0.263K	11.4	. . .
1NW272	2NW009	91	199	73.5	43.7	0.469K	12.1	AGN
1NW026	. . .	51	. . .	38.1	68.8	. . .	. . .	i?
1NW092	. . .	205	. . .	5.9	29.5	0.511B	12.4	. . .
1NW023	. . .	169	. . .	17.8	1.9	0.044B	9.9	. . .
1NW022	. . .	101	. . .	11.7	0.8	0.093K	10.4	. . .
1NW133	. . .	169	. . .	9.0	2.1	0.114H	10.7	AGN
. . .	2NW004	. . .	165	>39.5	<1.6	0.075H	10.2	. . .

Note.—Units of right ascension are hours, minutes, and seconds, and units of declination are degrees, arcminutes, and arcseconds.

[a] The letter suffixes represent the sources used: (K) Keck II/ESI data; (H) WIYN HYDRA data; and (B) A. Barger (2003, private communication).

[b] The natures are (i) interacting galaxy system from Fig. 7; (HII) sources with H II region–like spectra; and (AGN) sources with AGN/LINER–like spectra or radio excess. See § 4.3 for details.

[c] An alternative ID is an $R = 19.6$ galaxy at $z = 0.586$, which is known to be an X-ray source at R.A. = $10^{\mathrm{h}}53^{\mathrm{m}}39^{\mathrm{s}}.70$, decl. = $+57^{\circ}31'05''.0$ (J2000.0) (Lehmann et al. 2001).

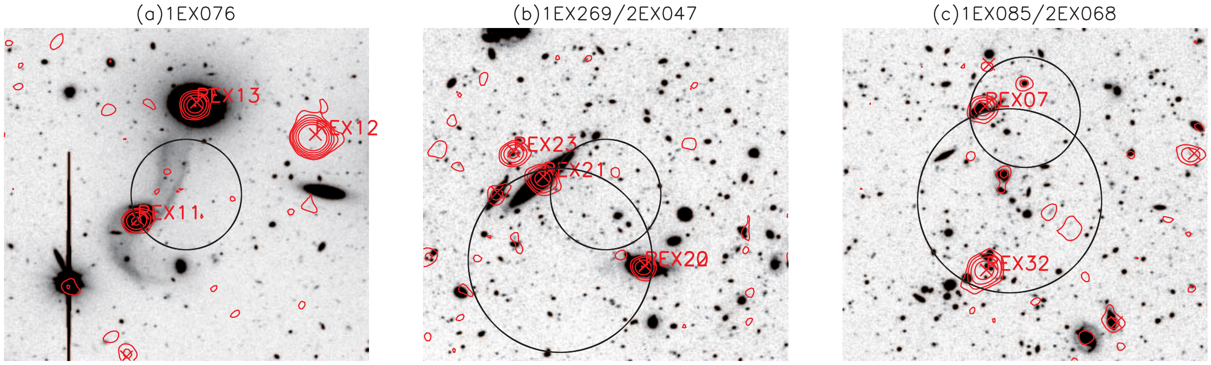

FIG. 8.—Wide *R*-band images ($2' \times 2'$) for a detailed explanation of the identification of (*a*) 1EX076, (*b*) 1EX269/2EX047, and (*c*) 1EX085/2EX068. Red contours and crosses are the same as in Fig. 7. The small and large circles show the 1 σ positional error of the 90 μm sources and the 170 μm sources, respectively.

candidates meeting the criterion, while 2NW006 [$F^C(170\ \mu\mathrm{m}) = 158$ mJy; R.A. $= 10^{\mathrm{h}}35^{\mathrm{m}}17\overset{\mathrm{s}}{.}0$, decl. $= +57°33'22''$ (J2000.0)] is identified with a relatively bright radio source [$F(1.4\ \mathrm{GHz}) = 2587\ \mu$Jy; R.A. $= 10^{\mathrm{h}}35^{\mathrm{m}}23\overset{\mathrm{s}}{.}30$, decl. $= +57°32'49\overset{''}{.}6$ (J2000.0)]. The separation between 1NW025 and 2NW006 is only $8''$. Since the identified source is too far (3.6 σ_{pos}) from the 1NW025 position, we regard 1NW025/2NW006 as unidentified.

4. DISCUSSION

4.1. *Redshift and FIR Luminosity*

The spectroscopic redshifts of 29 out of the 44 FIR sources in Table 4 are available. Twenty-five optical spectra of FIR sources were obtained with the Keck II and WIYN telescopes, while the redshifts of four objects (1NW062, 1NW100, 1NW092, and 1NW044) were kindly provided to us by A. Barger (2003, private communication). The 25 optical spectra are shown in Figure 9.

The redshift distributions of all FIR sources and 170 μm–detected FIR sources are shown in Figure 10 by open and filled histograms. Although more distant sources are expected at 170 μm than at 90 μm because of the strong *k*-correction brightening for dust emission, there are no significant differences in the redshift distribution between the sources detected at 170 μm and the sources detected only at 90 μm. Seven out of 12 (58%) of the 170 μm–detected sources and 19 out of the 27 (70%) 90 μm–only-detected sources lie at $z < 0.3$. This may be attributed to the small number statistics. Patris et al. (2003) reported that 95% (20/21) of 170 μm sources brighter than 200 mJy found in their FIRBACK southern Marano fields are at $z < 0.3$. Our 170 μm sources are slightly more distant than theirs, although their flux limit and their cumulative number density down to this limit are similar to ours. Their radio survey is shallower, using a larger observing beam, and these and other aspects of their source identification procedure might have introduced a bias toward optically bright foreground sources.

The redshift versus IR color relation is plotted in Figure 11 for our *ISO* FIR sources, together with the expectation from graybodies with λ^{-1} and λ^{-2} emissivities at $z = 0$–10. Most *ISO* FIR sources with 170 μm detection have a dust temperature ranging from 20 to 30 K for λ^{-1} and from 15 to 25 K for λ^{-2}, which is consistent with the temperature distribution of 74 ELAIS sources derived from the 170 μm/90 μm color (Héraudeau et al. 2004).

The FIR flux, $F_{\mathrm{FIR}}(40\text{–}500\ \mu\mathrm{m})$, can be estimated from the graybody fitting with the observed $F^C(90\ \mu\mathrm{m})$ and $F^C(170\ \mu\mathrm{m})$, the temperature from Figure 11, and the assumption of λ^{-2} emissivity. Adopting a different dust emissivity, λ^{-1}, increases F_{FIR} by 15% on average. This assumption does not change the main conclusion of this paper. It should be noted that the detection limits (43 mJy at 90 μm and 102 mJy at 170 μm after the correction for the flux bias) are substituted into the undetected band for the objects detected only in one band.

The FIR luminosity L_{FIR} is then obtained as

$$L_{\mathrm{FIR}} = 4\pi D_L^2 F_{\mathrm{FIR}}, \tag{13}$$

where D_L is the luminosity distance. The resulting FIR luminosity is given in Table 4 and plotted in Figure 12 as a function of redshift. Our sample consists of 24 sources with $L_{\mathrm{FIR}} < 10^{12}\ L_\odot$, 4 with $L_{\mathrm{FIR}} = 10^{12}$–$10^{13}\ L_\odot$, and 1 with $L_{\mathrm{FIR}} > 10^{13}\ L_\odot$. In the *IRAS* bright source catalog, only 6 out of 324 sources have $L_{\mathrm{FIR}} > 10^{12}\ L_\odot$ (Soifer et al. 1987). Thus, the fraction of $L_{\mathrm{FIR}} > 10^{12}\ L_\odot$ sources is 10 times greater in our *ISO* sample than in the *IRAS* bright source catalog. All the *IRAS* bright sources lie within $z \leq 0.1$, while only 10 of 29 sources are at $z \sim 0.1$ in our *ISO* sample. It is noted here that our spectroscopy project is not complete yet, and all the sources with $L(90\ \mu\mathrm{m})/L(R) > 50$ are left unobserved. It is generally agreed that sources with $L(90\ \mu\mathrm{m})/L(R) > 50$ belong to a population of ultraluminous infrared galaxies (ULIRGs) with $L_{\mathrm{FIR}} > 10^{12}\ L_\odot$. Hence, our sample should contain a greater fraction of $L_{\mathrm{FIR}} > 10^{12}\ L_\odot$ sources than that derived from our current spectroscopic knowledge.

4.2. *Luminosity Functions*

Here we derive the luminosity functions of our *ISO* FIR sources with $F^C(90\ \mu\mathrm{m}) \geq 85$ mJy. These new criteria are more strict than those used to identify sources with $F^C(90\ \mu\mathrm{m}) \geq 43$ mJy or $F^C(170\ \mu\mathrm{m}) \geq 102$ mJy. The reason for using the new criteria is to control the detection limit of our *ISO* FIR sources simply and to avoid the large correction for the completeness of the sample. Twenty-seven out of 44 galaxies identified with *ISO* FIR sources meet the new criteria, and redshifts of 21 sources are available.

The luminosity function $d\Phi(L_{\mathrm{FIR}})/dL_{\mathrm{FIR}}$ (i.e., the volume density of galaxies per unit luminosity range) is derived by following the $1/V_{\max}$ method as described in Schmidt (1968) and Eales (1993). The volume density of galaxies with luminosity between L and $L + dL$ is defined as

$$\frac{d\Phi(L_{\mathrm{FIR}})}{dL_{\mathrm{FIR}}} dL_{\mathrm{FIR}} = \sum_j \frac{1}{p(F^C)V_j}, \tag{14}$$

where $p(F^C)$ is the detection probability for a source with corrected flux F^C and the summation is over all sources with luminosity between L and $L + dL$ in the sample. The quantity $p(F^C)$ is obtained by combining the detection rate given by

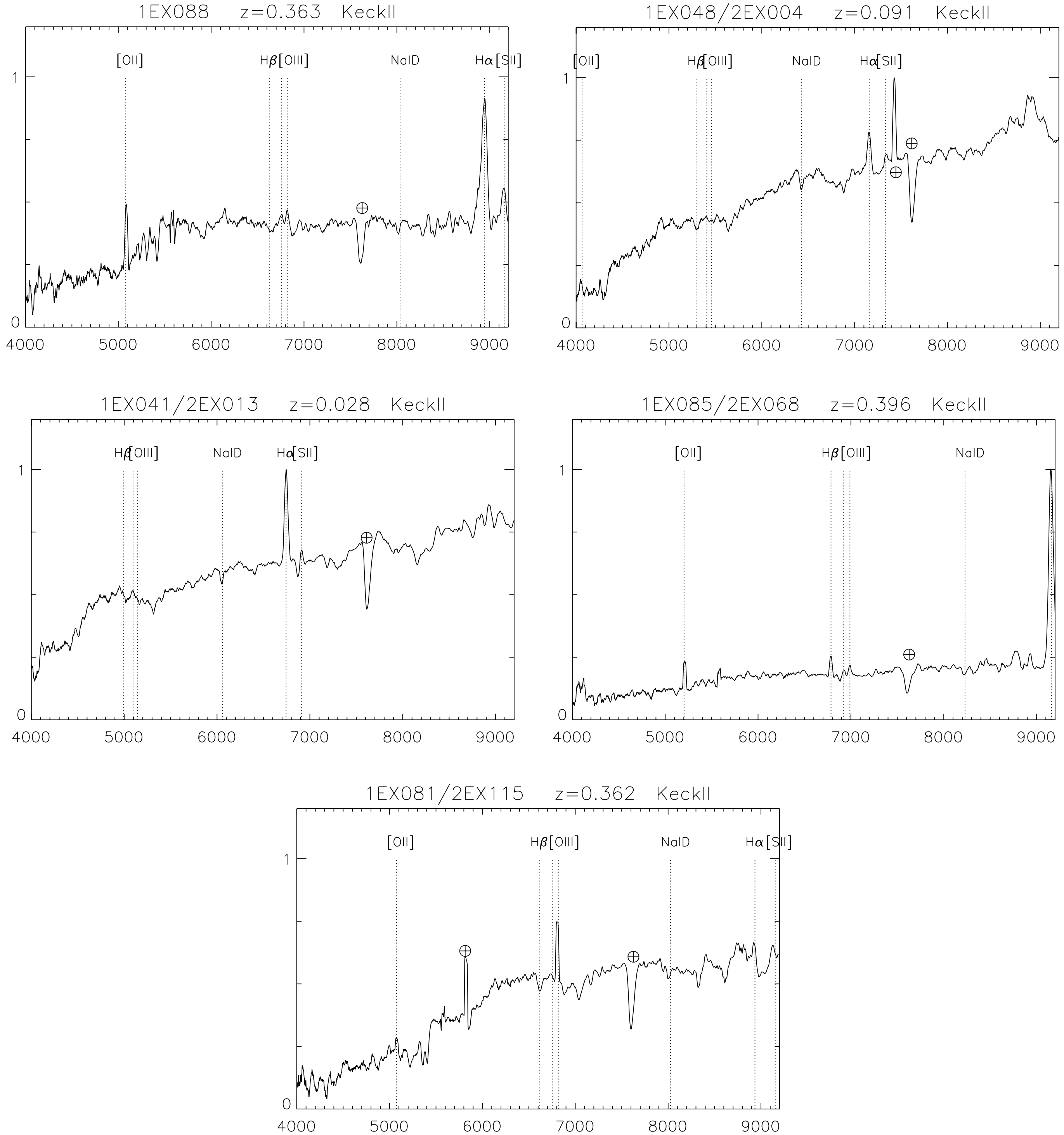

FIG. 9.—Optical spectra of *ISO* FIR sources. The wavelength is given in angstroms, and the vertical axis is in arbitrary units. Regions with bad pixels, residuals of night sky emission, and atmospheric absorptions are marked with Earth symbols.

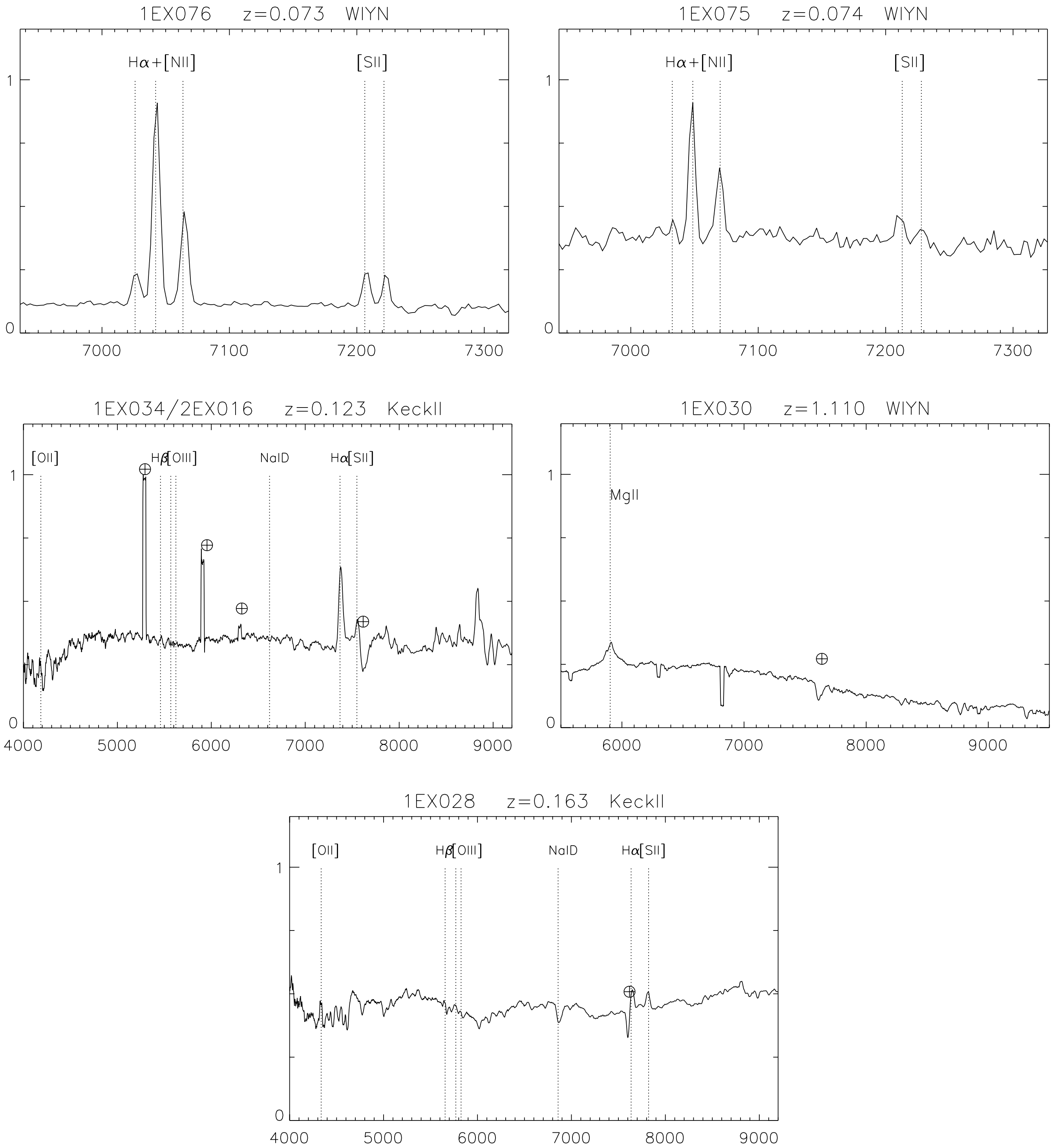

FIG. 9.—*Continued*

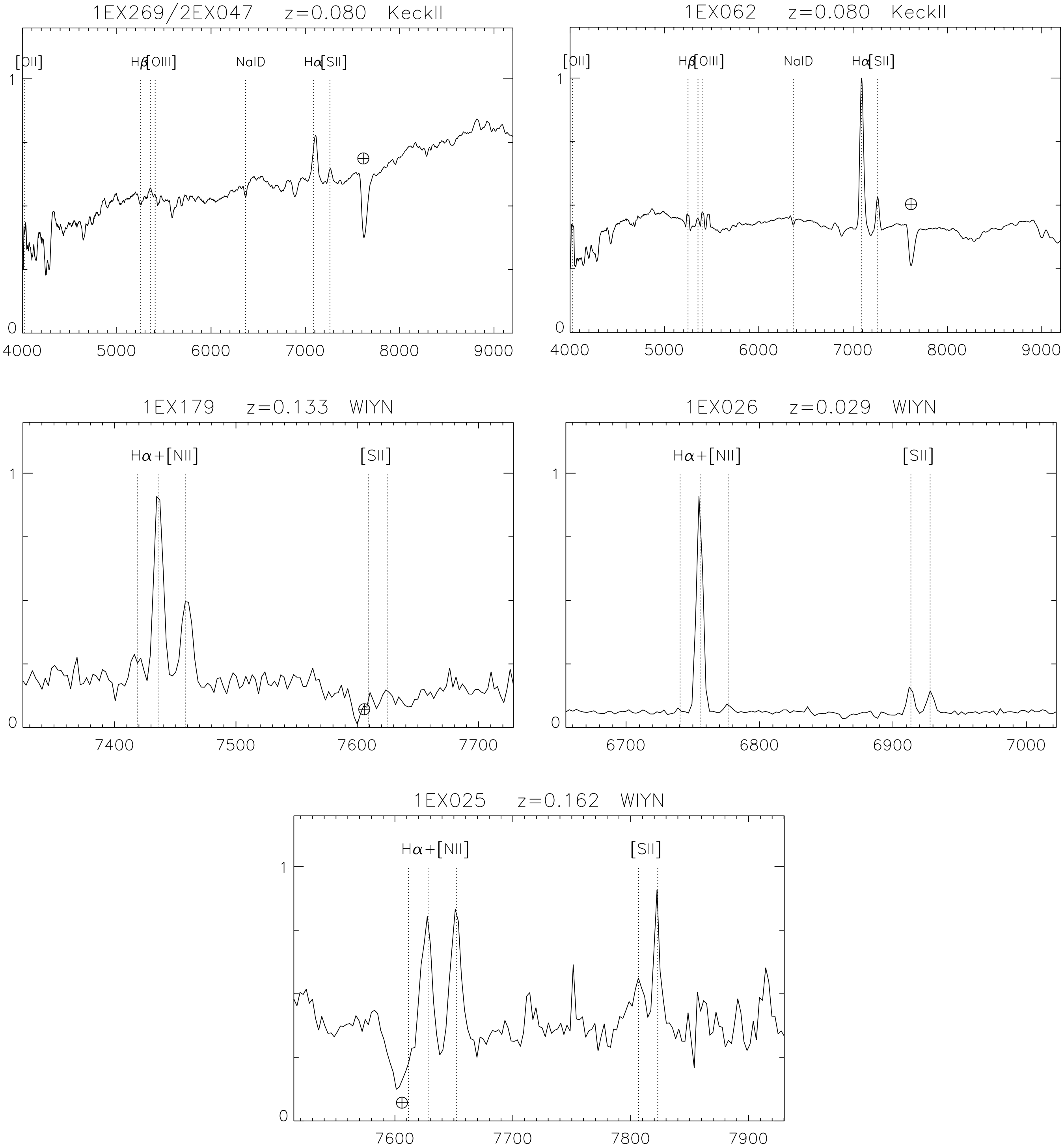

Fig. 9.—*Continued*

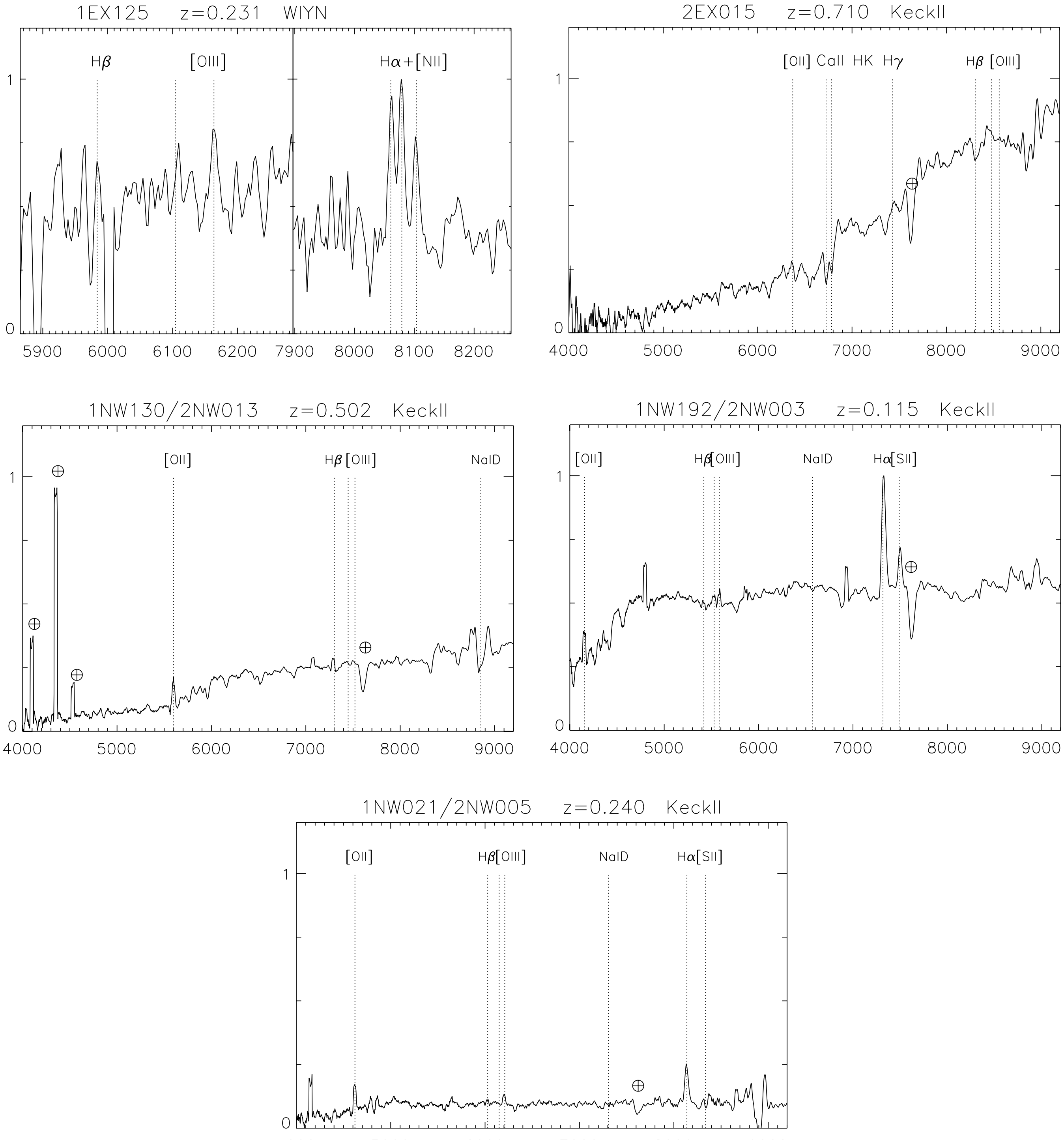

Fig. 9.—*Continued*

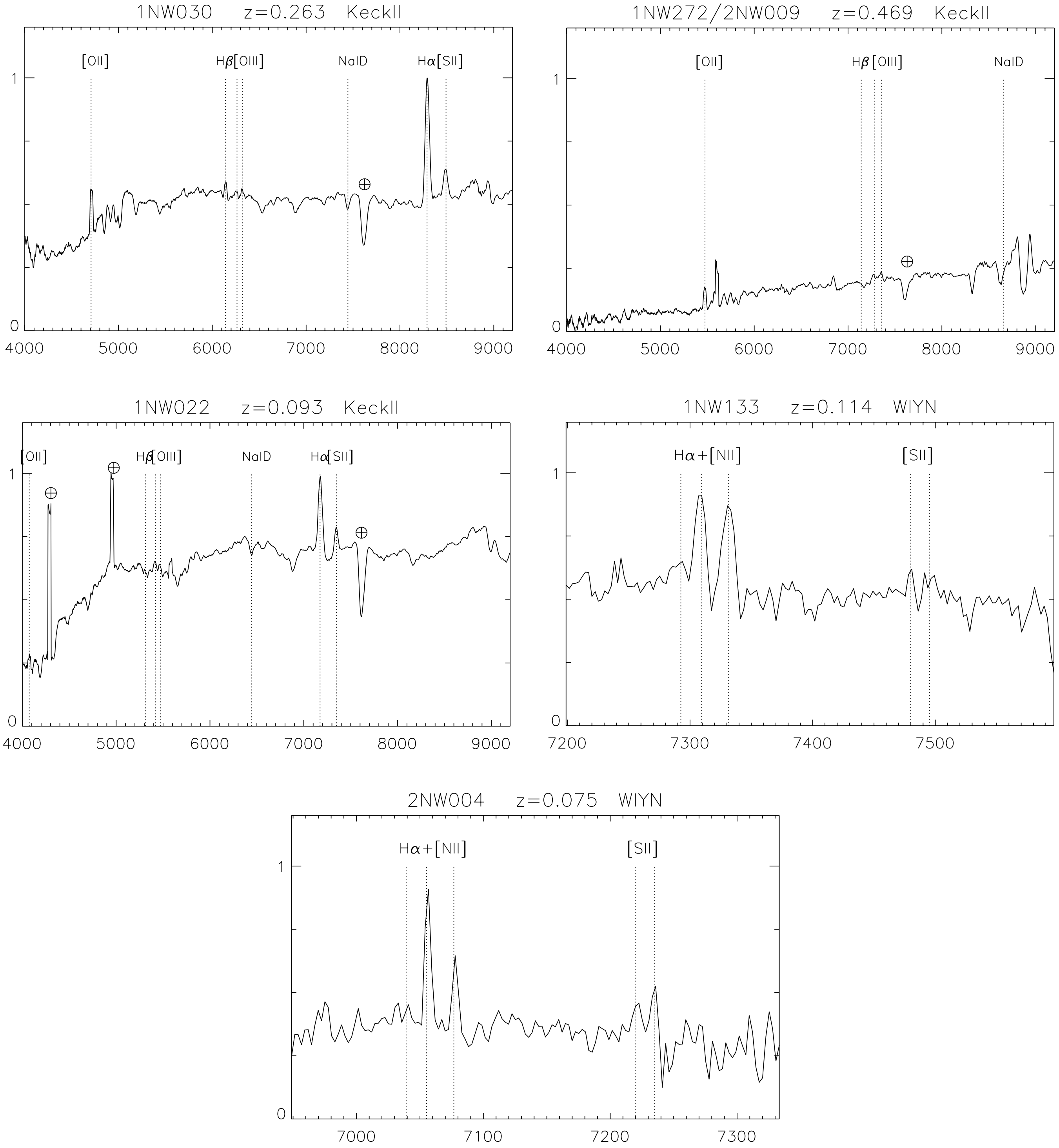

FIG. 9.—*Continued*

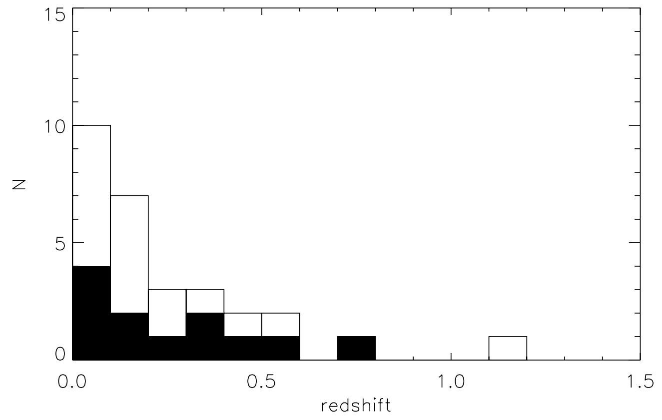

Fig. 10.—Redshift distributions of *ISO* FIR sources in the Lockman Hole. The open histogram shows all the sources, while the filled histogram plots the 170 μm–detected sources.

Figure 3 in Kawara et al. (2004) with equation (1) for transforming the observed flux F to the corrected flux F^C. Also, V_j is defined as

$$V_j = \int_\Omega \int_{z_{\rm min}}^{z_{\rm max}} \frac{d^2V}{d\Omega\, dz}\, dz\, d\Omega, \qquad (15)$$

where Ω is the solid angle in this survey, $d^2V/d\Omega\, dz$ is the comoving volume element, and $z_{\rm max}$ is the maximum redshift defined by the limiting fluxes at the faintest end, namely, $F^C(90\ \mu{\rm m}) = 85$ mJy, while $z_{\rm min}$ is the minimum redshift by the flux limits at the brightest end, which is set to 1 Jy for 90 μm. The luminosity functions are derived for three redshift bins: $z = 0.03–0.10$, 0.10–0.30, and 0.30–0.60. These redshift bins correspond to the different FIR luminosities, $L_{\rm FIR} = (0.7–7.4) \times 10^{10}$, $(5.4–28) \times 10^{10}$, and $(51–240) \times 10^{10}\ L_\odot$, respectively. The reason is that the luminosities of the *ISO* FIR sources are functions of redshift (see Fig. 12). The numbers of objects in each bin are six, seven, and five, and three sources that have $F^C(90\ \mu{\rm m}) \geq 85$ mJy are out of these three bins; two of them are at $z < 0.03$, and the other is at $z = 1.1$. The luminosity function also requires that $z_{\rm max}$ be no greater than z_u and that $z_{\rm min}$ be no less than z_l, where z_u and z_l are the maximum and minimum redshifts of the specific redshift bin.

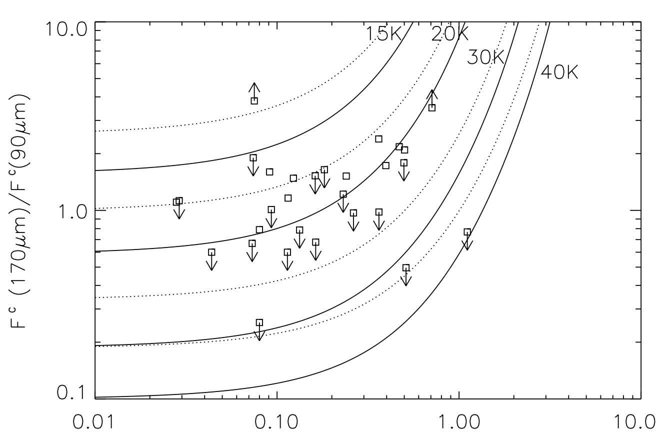

Fig. 11.—Redshift vs. flux ratio $F^C(170\ \mu{\rm m})/F^C(90\ \mu{\rm m})$. Solid and dotted lines show the expectation from a single-temperature blackbody multiplied by a $\lambda^{-\beta}$ emissivity. The calculations are made for temperatures of 15, 20, 30, and 40 K. Solid lines plot the flux ratios for a λ^{-2} emissivity, and dashed lines a λ^{-1} emissivity.

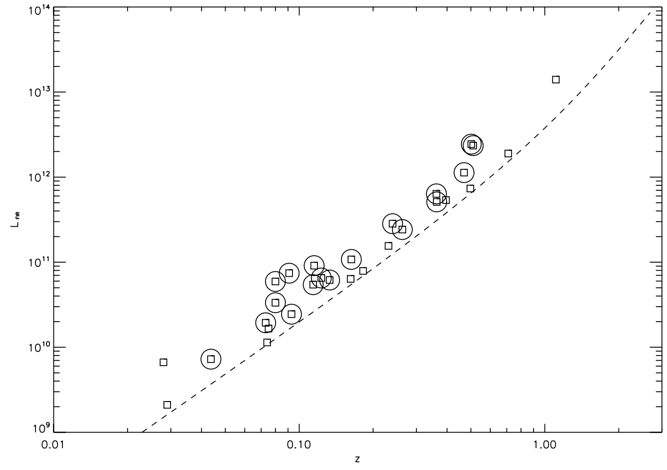

Fig. 12.—Relation of $L_{\rm FIR}$ to redshift. Squares with no circle denote sources that are not used to derive the luminosity function of the *ISO* FIR sources, because they are either too faint or outside the redshift bins. The dashed line shows our detection limits for the *ISO* FIR observations.

The luminosity function of our *ISO* FIR source sample is given in Table 5. Figure 13 compares the *ISO* FIR source sample with other galaxy samples. These results are calculated by summing up $1/p(F^C)V_j$ of the sources with a redshift (eq. [14]). Spectroscopic redshifts are obtained for 78% (21/27) of this sample, and no correction by a factor of 1.3 (27/21) was applied in Table 5 and Figure 13. The six *ISO* FIR sources without redshift are not expected to be in the same populations as our 21 *ISO* FIR sources with redshift, because the six sources without redshift tend to have higher $L(90\ \mu{\rm m})/L(R)$ than in the redshift-measured sources; sources without redshift have the range $30 < L(90\ \mu{\rm m})/L(R) < 1400$, while the 20 redshift-measured sources have $1 \lesssim L(90\ \mu{\rm m})/L(R) \lesssim 20$, and 1 source at $z = 0.469$ has $L(90\ \mu{\rm m})/L(R) = 43.7$.

The comparison includes the *IRAS* bright galaxy sample by Soifer et al. (1987) with a mean redshift of $\langle z \rangle \sim 0.04$, the *IRAS* 1 Jy ULIRG sample by Kim & Sanders (1998) with $\langle z \rangle \sim 0.15$, and the SCUBA galaxy sample by Barger et al. (2000) at $z = 1–3$. Here we assume that the infrared luminosity $L_{\rm IR}$ (8–1000 μm) is nearly equal to the FIR luminosity $L_{\rm FIR}$ (40–500 μm). The comparison shows a clear trend for the evolutionary effect; at a given luminosity, there is a greater density of galaxies for a higher redshift. It is particularly clear that there is a rapid evolution in the ULIRG population toward high redshift; the space densities are 1×10^{-7} Mpc^{-3} at $\langle z \rangle \sim 0.04$ (Soifer et al. 1987), 5×10^{-7} Mpc^{-3} at $\langle z \rangle \sim 0.15$ (Kim & Sanders 1998), and 4.6×10^{-5} Mpc^{-3} at $z = 0.3–0.6$. In other words, relative to the local universe, the space densities are ~5 times greater at $\langle z \rangle \sim 0.15$ and ~460 times greater at $z = 0.3–0.6$. At the highest end of the FIR luminosity, the space densities are 1000 times greater at $z = 1–3$ than in the local universe.

There is uncertainty in the flux calibration of our *ISO* FIR sources. Our flux calibration was done with an *IRAS* source (UGC 06009) that had ~50% flux errors (Kawara et al. 2004). This uncertainty brought the systematic luminosity shift to 0.3 dex in Figure 13. However, even if there were a 0.3 dex shift to lower luminosity, the evolution of the *ISO* FIR sources, especially at $z = 0.3–0.6$, would still exist. In addition, we compared the 90 μm luminosity function of the ELAIS (Serjeant et al. 2004). Serjeant et al. (2004) state that the *ISO* 90 μm luminosity function of the ELAIS is consistent with the *IRAS* survey, with the

TABLE 5

Luminosity Function Parameters of *ISO* FIR Sources

Parameter	$z = 0.03-0.10$	$z = 0.10-0.30$	$z = 0.30-0.60$
$L_{\rm FIR}$ (10^{10} $L_\odot$)	0.7–7.4	5.4–28	51–240
$N^{\rm a}$	6	7	5
$\frac{d\Phi}{d\log L}^{\rm b}$ (Mpc^{-3} dex^{-1})	$(1.9 \pm 0.9) \times 10^{-3}$	$(4.6 \pm 1.3) \times 10^{-4}$	$(4.6 \pm 1.3) \times 10^{-5}$

[a] Number of objects used to derive the space densities.

[b] Error from Poisson statistics.

assumption of pure luminosity evolution of $(1+z)^3$. If we apply their pure luminosity evolution of $(1+z)^3$ to our data, at least our luminosity functions at $z = 0.03-0.1$ and 0.1–0.3 are consistent with those of the ELAIS and *IRAS* bright galaxy samples. On the other hand, the luminosity function at $z = 0.3-0.6$ shows a luminosity excess by a factor of ~2 over that of the *IRAS* bright galaxy sample after luminosities are reduced by a factor of $(1+z)^3$. This suggests a much stronger evolution for the *ISO* FIR sources at this redshift range, at which ELAIS can barely observe. It is noted again that our spectroscopic observations miss almost all sources with $L(90\ \mu{\rm m})/L(R) > 30$, many of which would belong to a population of ULIRGs with $L_{\rm FIR} > 10^{12}\ L_\odot$. The space density of *ISO* FIR sources with $L_{\rm FIR} > 10^{12}\ L_\odot$, which is derived here, must be significantly underestimated.

4.3. *Nature of ISO FIR Sources*

The fraction of *ISO* FIR sources associated with an AGN is estimated from optical emission lines, radio continuum emission, and X-ray activity. The excitation diagnosis by Veilleux & Osterbrock (1987) is applied to the spectra of the *ISO* FIR sources for optical spectral classification. One object (1EX030) is a quasar with $L_{\rm FIR} = 10^{13.1}\ L_\odot$ at $z = 1.11$. Two objects (1EX025 and 1NW133) are type II Seyfert galaxies or LINERs with $L_{\rm FIR} = 10^{10.8}-10^{10.9}\ L_\odot$ at $z = 0.11-0.16$. Two objects (1EX026 and 1EX076) are H II galaxies with $L_{\rm FIR} = 10^{9.4}-10^{10.4}\ L_\odot$ at $z = 0.03-0.07$. The remaining galaxies are left unclassified because of poor wavelength coverage, spectral resolution, or quality of the spectrum. Optical images indicate that four galaxies and possibly another two are interacting systems. Their optical properties are summarized in Table 4.

The relationship between 1.4 GHz and FIR emission is examined in the $L(1.4\ {\rm GHz})/L(90\ \mu{\rm m})$ versus $F^C(170\ \mu{\rm m})/F^C(90\ \mu{\rm m})$ diagram as shown in Figure 14.[16] Open and filled squares represent sources lying in the LHEX and LHNW fields, respectively. The dashed and dotted lines show the redshift loci of two different types of ULIRGs, NGC 6240 (with an AGN) and Arp 220 (without an AGN) (e.g., Smith et al. 1998), while the dash-dotted line shows that of starburst galaxy M82. This figure indicates that most of the *ISO* FIR sources are pure star-forming or star formation–dominated galaxies, as they lie near the loci of Arp 220 and M82. Three optically classified AGNs, 1EX030, 1EX025, and 1NW133, also appear in the same area occupied by star formation–dominated objects. Three FIR sources, 1EX100, 1EX047/2EX036, and 1NW272/2NW009, are found near the locus of NGC 6240. Source 1NW272/2NW009 is classified as a type II AGN with $L_{\rm FIR} = 10^{12.2}\ L_\odot$ at $z = 0.47$. No spectroscopic data are available for the two other sources. The source 2EX015, which has the highest $L(1.4\ {\rm GHz})/L(90\ \mu{\rm m})$, is identified with a powerful radio galaxy at $z = 0.710$.

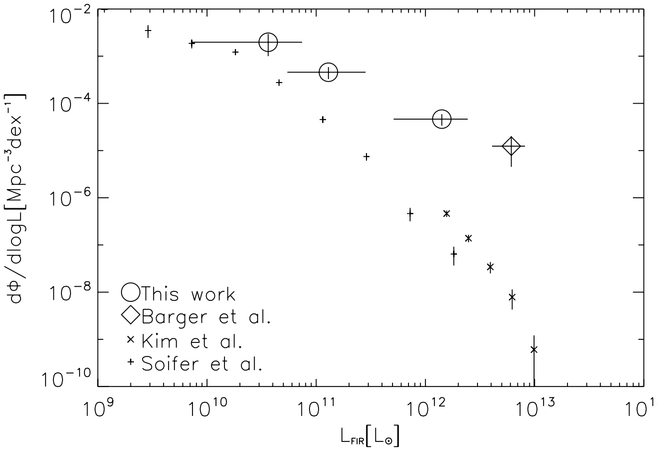

Fig. 13.—Comparison of the luminosity function of the *ISO* FIR source sample with other samples. Circles show the luminosity function of the *ISO* FIR source sample plotted in the redshift bins $z = 0.03-0.10$, 0.10–0.30, and 0.30–0.60 (*left to right*). Horizontal error bars represent the luminosity ranges of the subsample in the redshift bins, and vertical error bars represent the Poisson errors. Plus signs show the luminosity function of the *IRAS* bright galaxy sample at $\langle z \rangle \sim 0.04$ (Soifer et al. 1987), small crosses the *IRAS* 1 Jy ULIRG sample at $\langle z \rangle \sim 0.15$ (Kim & Sanders 1998), and diamonds the SCUBA source sample at $z = 1-3$ (Barger et al. 2000). In order to present the data of Soifer et al. (1987), Kim & Sanders (1998), and Barger et al. (2000), the infrared luminosity $L_{\rm IR}$ is assumed to be equal to $L_{\rm FIR}$.

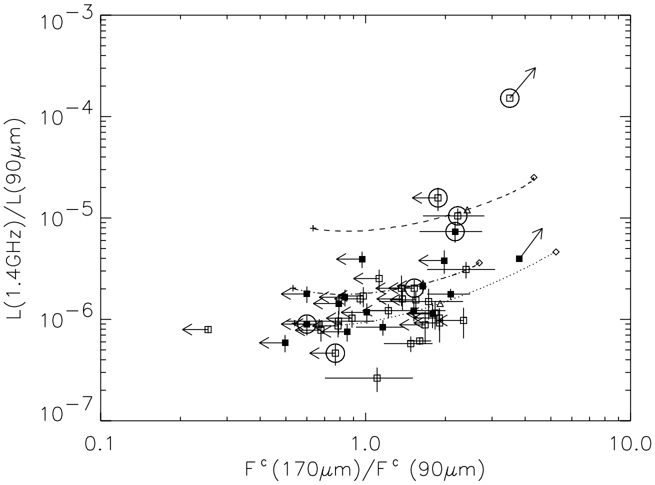

Fig. 14.—Relation of $F^C(170\ \mu{\rm m})/F^C(90\ \mu{\rm m})$ to $L(1.4\ {\rm GHz})/L(90\ \mu{\rm m})$. Open squares show sources in the LHEX field, while filled squares show those in the LHNW field. The seven large circles indicate galaxies showing AGN signatures. The dashed, dotted, and dash-dotted lines represent the loci of the redshifted SEDs of NGC 6240, Arp 220, and M82, respectively. The plus signs, triangles, and diamonds on the loci indicate $z = 0$, 1.0, and 2.0.

---

[16] The quantities $L(1.4\ {\rm GHz})$, $L(90\ \mu{\rm m})$, and $L(R)$ are monochromatic luminosities and are defined by $4\pi D_L^2 \nu f_\nu$, where D_L denotes the luminosity distance to the object.

As discussed so far, our sample contains at least seven galaxies hosting an AGN and five ULIRGs. Three AGN-host galaxies have FIR luminosities characteristic of ULIRGs. Thus, 60% (3/5) of our ULIRGs are AGN galaxies, in agreement with the fraction found in the *IRAS* sample (Sanders & Mirabel 1996), and this suggests that the fraction of AGN galaxies with an ULIRG luminosity does not change much from the local universe to $z \sim 0.5$. Deep X-ray surveys have been conducted in the LHEX field by the *ROSAT* and *XMM-Newton* satellites (e.g., Lehmann et al. 2001; Mainieri et al. 2002). If our seven AGNs have X-ray-to-FIR luminosity ratios $L_X/L_{\rm FIR}$ similar to those of AGN-associated ULIRGs such as NGC 6240 and Mrk 231, then 2×10^{-15} and 6×10^{-15} ergs cm^{-2} s^{-1} are expected at the 0.5–2 and 2–10 keV energy bands, respectively, for objects with 100 mJy at 100 μm. Out of our seven AGN galaxies, only one source, 1EX030, identified as a quasar, has been detected in the X-ray. Two undetected sources lie within the *ROSAT* Deep Survey area with a flux limit of 10×10^{-15} ergs cm^{-2} s^{-1}, and it is not surprising that these galaxies were not detected by *ROSAT*. The powerful radio galaxy 2EX015 at $z = 0.710$ and another AGN candidate, 1EX110 (which has no optical spectrum yet), are found within the *XMM-Newton* survey area with a limiting flux of 1.4×10^{-15} ergs cm^{-2} s^{-1} in the 2–10 keV energy band. The X-ray nondetection of these two objects may be attributed to a Compton thick absorber with a column density of 3×10^{24} cm^{-2}, which is equivalent to $A_V \sim 1200$ mag. The two remaining AGN sources are outside the X-ray survey area. It is interesting that the fraction of AGN host galaxies detected by the deep X-ray surveys is rather small. This is also a nice demonstration that the combination of FIR and radio observations offers a powerful tool for finding heavily obscured AGNs that might be difficult to find in the X-ray.

The 90 μm luminosity relative to the optical *R*-band luminosity, $L(90\ \mu{\rm m})/L(R)$, is plotted against optical color, $R - I$, in Figure 15. The large diamond and square show the FIRBACK 170 μm sources, FN1-40 at $z = 0.449$ and FN1-64 at $z = 0.907$ (Chapman et al. 2002). The loci expected from the SEDs of NGC 6240, Arp 220, and M82 at $z = 0$–2 are shown using dashed and dotted lines. This figure demonstrates that the *ISO* succeeded in detecting objects with a wide range of $L(90\ \mu{\rm m})/L(R)$ ratios, from 1 to 1000, and shows a bimodal distribution for the $L(90\ \mu{\rm m})/L(R)$ of our *ISO* FIR sources. One peak, with $1 < L(90\ \mu{\rm m})/L(R) < 3$, appears to represent the population of normal star-forming galaxies in the nearby universe because of their brightness in the optical. The other peak with FIR excess represents infrared-dominant sources such as Arp 220, whose luminosity is nearly entirely reprocessed by dust. In Rodighiero et al. (2005), which reduced the same *ISO* data in the LHEX and made identification with radio and 15 μm sources (see the Appendix for details), 9 of 11 sources were fitted with the SEDs of M82 or M51, which are FIR-moderate galaxies, while two others have an Arp 220 SED. The number of Arp 220–like sources seems to be small; however, their SED template fitting was done for the sources whose redshifts were available. Thus, there might be a bias to optically bright sources.

Figure 15 also shows that there is possibly a third class of objects with an extreme excess of FIR luminosity, $L(90\ \mu{\rm m})/L(R) > 500$. Although ULIRGs are known to have the largest intrinsic excess of FIR luminosity relative to optical luminosity, their extreme optical and FIR colors cannot be adequately explained by simply redshifting the observed SEDs of ULIRGs or starburst galaxies. Therefore, the five such objects, one from FIRBACK and four from our survey, may represent a new population of extreme FIR-excess galaxies. If the extreme values of $L(90\ \mu{\rm m})/L(R)$ are intrinsic, the small optical luminosity may imply that their stellar system has not been fully developed or that their entire stellar structures are heavily obscured by dust.

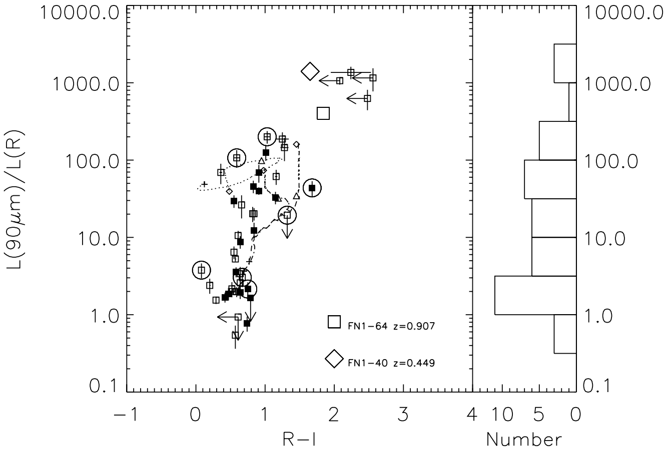

Fig. 15.—*Left*: The 90 μm luminosity relative to the optical *R*-band luminosity plotted against the optical $R - I$ color. The symbols are the same as in Fig. 14 but with a large square and diamond showing the infrared-luminous galaxies FN1-64 and FN1-40, from the FIRBACK survey (Chapman et al. 2002). *Right*: Number distribution as a function of $L(90\ \mu{\rm m})/L(R)$.

Four such objects in the Lockman Hole fields are located on the outside of the field, where the submillimeter and millimeter observations with SCUBA, Bolocam, and MAMBO (Scott et al. 2002; Greve et al. 2004; Laurent et al. 2005) were performed. In the future, the measurements at such a wavelength will give additional information. In addition, one of the *Spitzer Space Telescope* Legacy Programs, SWIRE (Lonsdale et al. 2003), covers these fields in the wavelengths from 3.6 to 160 μm, and those data will be released and help to understand such objects.

5. SUMMARY

By exploiting the FIR-radio correlation, we have performed a likelihood-ratio analysis to identify the FIR sources that have been found in an area of $\sim$0.9 deg^2 during the *ISO* deep FIR survey in the Lockman Hole. New observations have been conducted to construct catalogs of radio and optical objects, which include a deep VLA 1.4 GHz observation, optical *R*- and *I*-band imaging on the Subaru 8 m and UH 2.2 m telescopes, and optical spectroscopy on the Keck II 10 m and WIYN 3.5 m telescopes. A summary of the results presented in this paper is as follows:

1. Our samples of 116 and 20 sources are selected with the criteria of $F^C(90\ \mu{\rm m}) \geq 43$ mJy and $F^C(170\ \mu{\rm m}) \geq 102$ mJy, respectively. Our 1.4 GHz radio sample includes a total of 463 sources.
2. In order to remove positional coincidence by chance, we calculate the likelihood ratio and the reliability. As a result, 44 FIR sources are identified with radio sources.
3. Optical confirmation of the 44 FIR/radio associations is conducted using accurate radio positions. The dispersion in the difference between the radio and optical positions is $0\farcs6$.
4. Dust temperature is derived from the FIR color ranges between 15 and 30 K.
5. Spectroscopic redshifts have been obtained for 29 out of the 44 identified sources. There are no significant differences in the redshift between 170 μm–detected sources and 90 μm–only-detected sources.

6. Twenty-four (out of 29) FIR galaxies with redshifts have $L_{\rm FIR} < 10^{12}\ L_\odot$, 4 have $L_{\rm FIR} = 10^{12}$–$10^{13}\ L_\odot$, and 1 has $L_{\rm FIR} > 10^{13}\ L_\odot$.

7. The luminosity functions are calculated using the $1/V_{\rm max}$ method. The space density of our sample galaxies at $z = 0.3$–0.6 is 4.6×10^{-5} Mpc^{-3}, which is 460 times as high as that in the local universe. A rapid evolution in the ULIRG population is suggested.

8. Most *ISO* FIR sources have L(1.4 GHz)/L(90 μm) similar to that in the star-forming galaxies Arp 220 and M82, indicating that star formation is the dominant source of FIR and radio emission in these galaxies.

9. Our FIR sample contains at least seven AGNs, which are classified from either optical emission lines, excess in radio emission, or X-ray activity.

10. Three-fifths (60%) of our ULIRGs are AGN galaxies, implying that the percentage of AGN galaxies with ULIRG luminosity does not change significantly between $z = 0$ and $z \sim 0.6$.

11. Five of the seven AGN galaxies are within the *ROSAT* X-ray survey field, and two are within the *XMM-Newton* survey fields. X-ray emission has been detected in only one source, 1EX030, which is optically classified as a quasar. If our AGN galaxies had $L_{\rm X}/L_{\rm FIR}$ similar to that of NGC 6240, an ULIRG hosting an AGN, then none of our AGN galaxies would have been detected by *ROSAT.* The nondetection in the *XMM-Newton* 2–10 keV band implies a very thick absorption column density of 3×10^{24} cm^{-2} or $A_V \sim 1200$ mag obscuring the central source of the two AGN galaxies. The combination of FIR and radio observations would provide a powerful tool for finding heavily obscured AGNs that might be difficult to find in the X-ray.

12. Several sources show an extreme FIR luminosity relative to the optical R band, L(90 μm)/L(R) > 500. Such extreme values cannot be explained from the redshifted SEDs of ULIRGs and may imply a new population of galaxies with an extreme amount of star formation in an undeveloped stellar system. If so, we might be looking at the formation of bulges or elliptical galaxies.

We wish to thank the staff of the Subaru Observatory, NOAO, NRAO, Keck Observatory, and the UH 88 m telescope for their assistance and hospitality during the several observing runs that collected data for this paper. This research made use of the NASA/IPAC Extragalactic Database, which is operated by the Jet Propulsion Laboratory, California Institute of Technology, under contract with the National Aeronautics and Space Administration. This paper is based on observations with *ISO*, an ESA project with instruments funded by ESA member states and with the participation of ISAS and NASA. We thank the anonymous referee for comments that greatly improved our work.

APPENDIX

COMPARISON WITH RODIGHIERO ET AL.

Rodighiero et al. (2003) and Rodighiero & Franceschini (2004) have reduced our 90 μm data in the LHEX and LHNW fields with their own method, a parametric algorithm that fits the signal time history of each detector pixel. They then identified the singularities induced by cosmic-ray impacts and transient effects in the detectors and extracted real sky sources. The numbers of their sources with signal-to-noise ratio greater than 3 are 36 and 28 in the LHEX and LHNW, respectively, while our catalogs consist of 116 and 107 sources with signal-to-noise ratio greater than 3 (Kawara et al. 2004). Both catalogs are made with a different method. Thus, the reason for this difference is expected to be in the reduction and source-extracting methods, but this is unclear.

TABLE 6

Identification with Sources in Rodighiero et al.

	Rodighiero et al. (2003, 2004)		Kawara et al. (2004)	
ID[a]	Name	Flux (mJy)	Name	Flux (mJy)[b]
ex001	LHJ 105324+572921	95 ± 18	1EX026	90 ± 20
ex003[c]	LHJ 105349+570716	577 ± 110	1EX023	1218 ± 44
ex004	LHJ 105052+573507	224 ± 42	1EX041	310 ± 80
ex007	LHJ 105300+570548	169 ± 32	1EX062	399 ± 29
ex008	LHJ 105041+570708	126 ± 24	1EX048	254 ± 19
ex009	LHJ 105254+570816	145 ± 27	1EX269	206 ± 53
ex012	LHJ 105113+571415	91 ± 17	1EX081	88 ± 16
ex019	LHJ 105318+572130	63 ± 12	1EX179	129 ± 29
ex020	LHJ 105127+573524	49 ± 9	1EX076	152 ± 17
ex022[d]	LHJ 105223+570159	32 ± 6	1EX148	112 ± 29
ex025	LHJ 105206+570751	62 ± 12	1EX034	124 ± 18
ex027	LHJ 105328+571404	53 ± 10	1EX125	83 ± 12
ex028[d]	LHJ 105226+570222	27 ± 5	1EX148	112 ± 29
ex029	LHJ 105132+572925	45 ± 9	1EX100	54 ± 14
ex036	LHJ 105323+571451	20 ± 4	1EX126	74 ± 16
nw001	LHJ 103521+580034	235 ± 24	1NW055	103 ± 19
nw002	LHJ 103606+574715	163 ± 17	1NW023	169 ± 31
nw003	LHJ 103604+574815	181 ± 20	1NW092	205 ± 38
nw006	LHJ 103515+573330	136 ± 16	1NW025	91 ± 20
nw008	LHJ 103318+574925	159 ± 19	1NW021	126 ± 23
nw011	LHJ 103530+573139	73 ± 12	1NW043	79 ± 17
nw012	LHJ 103409+572715	63 ± 10	1NW221	59 ± 11
nw016	LHJ 103610+574330	85 ± 14	1NW022	101 ± 22
nw020	LHJ 103249+573719	56 ± 11	1NW192	226 ± 33
nw026	LHJ 103316+573136	30 ± 10	1NW031	128 ± 28
nw027	LHJ 103327+574539	42 ± 12	1NW114	49 ± 16

[a] For the source IDs, the number follows the order of appearance in the respective catalog. The prefix "ex" signifies sources in Rodighiero et al. (2003), and "nw" signifies sources in Rodighiero & Franceschini (2004).

[b] These fluxes are corrected with eq. (1).

[c] This is the *IRAS* source UGC 06009, which is used for our flux calibration.

[d] Sources ex022 and ex028 may be blending with each other.

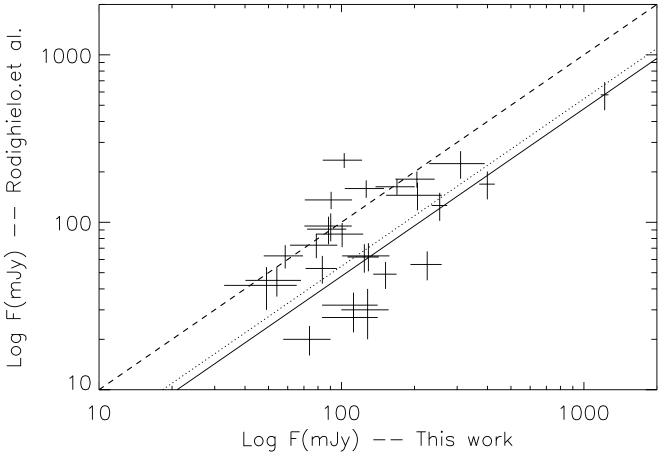

Fig. 16.—Comparison of our 90 μm fluxes with Rodighiero et al. (2003) and Rodighiero & Franceschini (2004). The solid line denotes the ratio of 2.1 that comes from the flux difference of the *IRAS* source. The mean ratio of our flux with those in Rodighiero et al. (2003) and Rodighiero & Franceschini (2004) is 1.8 (*dotted line*), and the dashed line shows a ratio of 1.0.

In Table 6 the 15 LHEX and 11 LHNW sources of Rodighiero et al. have a counterpart within 30″ in our catalogs. Figure 16 compares the Rodighiero et al. fluxes with ours. One *IRAS* source, UGC 06009, is reported as ex003 (577 ± 110 mJy) in Rodighiero et al. (2003), while we used this source for the flux calibration of the *IRAS* 100 μm measurement (1218 mJy). A difference of a factor of 2.1 between our fluxes and those of Rodighiero et al. might be expected, and the mean ratio of our fluxes and those in Rodighiero et al. (2003) and Rodighiero & Franceschini (2004) is 1.8. As shown in Figure 16, there are some sources in our catalog with ∼100 mJy that show much fainter fluxes in their catalogs, and these sources could make the deviation of the flux ratio bigger.

Rodighiero et al. (2005) have identified their 36 90 μm sources (Rodighiero et al. 2003) in the LHEX field using the association with the shallow radio (de Ruiter et al. 1997) and 15 μm sources (Fadda et al. 2004; Rodighiero et al. 2004). Seventeen of them are identified with radio and 15 μm sources, all of which are optically identified. Fourteen of the 17 optically identified sources are found in our catalog (Kawara et al. 2004), and we made the same optical identification in this paper. However, only 1 (ex002/1EX100) of their 19 optically unidentified sources is found in Kawara et al. (2004) and is successfully identified in this work. It is unclear why most of their unidentified sources are not found in Kawara et al. (2004).

REFERENCES

Barger, A. J., Cowie, L. L., & Richards, E. A. 2000, AJ, 119, 2092
Barger, A. J., Cowie, L. L., Sanders, D. B., Fulton, E., Taniguchi, Y., Sato, Y., Kawara, K., & Okuda, H. 1998, Nature, 394, 248
Blain, A. W., Kneib, J. P., Ivison, R. J., & Smail, I. 1999, ApJ, 512, L87
Chapman, S. C., Smail, I., Ivison, R. J., Helou, G., Dale, D. A., & Lagache, G. 2002, ApJ, 573, 66
Condon, J. J. 1992, ARA&A, 30, 575
de Ruiter, H. R., Arp, H. C., & Willis, A. G. 1977, A&AS, 28, 211
de Ruiter, H. R., et al. 1997, A&A, 319, 7
Eales, S. 1993, ApJ, 404, 51
Efstathiou, A., et al. 2000, MNRAS, 319, 1169
Fadda, D., Lari, C., Rodighiero, G., Franceschini, A., Elbaz, D., Cesarsky, C., & Perez-Fournon, I. 2004, A&A, 427, 23
Fixsen, D. J., Dwek, E., Mather, J. C., Bennett, C. L., & Shafer, R. A. 1998, ApJ, 508, 123
Flores, H., et al. 1999, ApJ, 517, 148
Franceschini, A., Aussel, H., Cesarsky, C. J., Elbaz, D., & Fadda, D. 2001, A&A, 378, 1
Greve, T. R., Ivison, R. J., Bertoldi, F., Stevens, J. A., Dunlop, J. S., Lutz, D., & Carilli, C. L. 2004, MNRAS, 354, 779
Hasinger, G., Burg, R., Giacconi, R., Schmidt, M., Trumper, J., & Zamorani, G. 1998, A&A, 329, 482
Hauser, M. G., et al. 1998, ApJ, 508, 25
Héraudeau, P., et al. 2004, MNRAS, 354, 924
Holland, W. S., et al. 1999, MNRAS, 303, 659
Hughes, D., et al. 1998, Nature, 394, 241
Kawara, K., et al. 1998, A&A, 336, L9
———. 2004, A&A, 413, 843
Kessler, M. F., et al. 1996, A&A, 315, L27
Kim, D. C., & Sanders, D. B. 1998, ApJS, 119, 41
Landolt, A. U. 1992, AJ, 104, 340
Laurent, G. T., et al. 2005, ApJ, 623, 742
Lehmann, I., et al. 2001, A&A, 371, 833
Lemke, D., et al. 1996, A&A, 315, L64
Lockman, F. J., Jahoda, K., & McCammon, D. 1986, ApJ, 302, 432
Lonsdale, C. J., et al. 2003, PASP, 115, 897
Luppino, G., et al. 1996, in ASP Conf. Ser. 88, Clusters, Lensing, and the Future of the Universe, ed. V. Trimble & A. Reisenegger (San Francisco: ASP), 229
Mainieri, V., Bergeron, J., Hasinger, G., Lehmann, I., Rosati, P., Schmidt, M., Szokoly, G., & Della Ceca, R. 2002, A&A, 393, 425
Majewski, S. R., Kron, R. G., Koo, D. C., & Bershady, M. A. 1994, PASP, 106, 1258
Mann, R. G., et al. 1997, MNRAS, 289, 482
———. 2002, MNRAS, 332, 549
Matsuhara, H., et al. 2000, A&A, 361, 407
Miyazaki, S., et al. 2002, PASJ, 54, 833
Monet, D., et al. 1998, USNO-A2.0 Catalog (Flagstaff: USNO)
Patris, J., Dennefeld, M., Lagache, G., & Dole, H. 2003, A&A, 412, 349
Puget, J.-L., Abergel, A., Bernard, J.-P., Boulanger, F., Burton, W. B., Desert, F.-X., & Hartmann, D. 1996, A&A, 308, L5
Puget, J. L., Lagache, G., & Clements, D. L. 1999, A&A, 345, 29
Richards, E. A. 2000, ApJ, 533, 611
Rodighiero, G., Fadda, D., Franceschini, A., & Lari, C. 2005, MNRAS, 357, 449
Rodighiero, G., & Franceschini, A. 2004, A&A, 419, L55
Rodighiero, G., Lari, C., Fadda, D., Franceschini, A., Elbaz, D., & Cesarsky, C. 2004, A&A, 427, 773
Rodighiero, G., Lari, C., Franceschini, A., Greganin, A., & Fadda, D. 2003, MNRAS, 343, 1155
Rowan-Robinson, M., et al. 1991, Nature, 351, 719
———. 1997, MNRAS, 289, 490
Rutledge, E. R., Brunner, R. J., Prince, T. A., & Lonsdale, C. 2000, ApJS, 131, 335
Sanders, D. B., & Mirabel, I. F. 1996, ARA&A, 34, 749
Schmidt, M. 1968, ApJ, 151, 393
Scott, S. E., et al. 2002, MNRAS, 331, 817
Serjeant, S., et al. 2004, MNRAS, 355, 813
Sheinis, A. I., Miller, J. S., Bolte, M., & Sutin, B. 2000, Proc. SPIE, 4008, 522
Smail, I., Ivison, R. J., & Blain, A. W. 1997, ApJ, 490, L5
Smith, H. E., Lonsdale, C. J., Lonsdale, C. J., & Diamond, P. J. 1998, ApJ, 493, L17
Soifer, B. T., Sanders, D. B., Madore, B. F., Neugebauer, G., Danielson, G. E., Elias, J. H., Lonsdale, C. J., & Rice, W. L. 1987, ApJ, 320, 238
Stetson, P. B. 1987, PASP, 99, 191
Sutherland, W., & Saunders, W. 1992, MNRAS, 259, 413
Takeuchi, T. T., Ishii, T. T., Hirashita, H., Yoshikawa, K., Matushara, H., Kawara, K., & Okuda, H. 2001, PASJ, 53, 37
Totani, T., & Takeuchi, T. T. 2002, ApJ, 570, 470
Totani, T., Yoshii, Y., Iwamuro, F., Maihara, T., & Motohara, K. 2001, ApJ, 550, L137
Valdes, F. 1995, Guide to the HYDRA Reduction Task DOHYDRA (Tucson: NOAO), http://iraf.noao.edu
Veilleux, S., & Osterbrock, D. E. 1987, ApJS, 63, 295
Wolstencroft, R. D., Savage, A., Clowes, R. G., MacGillivray, H. T., Leggett, S. K., & Kalafi, M. 1986, MNRAS, 223, 279
Yun, M. S., Reddy, N. A., & Condon, J. J. 2001, ApJ, 554, 803